Enriching the symphony of gravitational waves from binary black holes by tuning higher harmonics

Roberto Cotesta,[1,*] Alessandra Buonanno,[1,2] Alejandro Bohé,[1] Andrea Taracchini,[1] Ian Hinder,[1] and Serguei Ossokine[1]

[1]*Max Planck Institute for Gravitational Physics (Albert Einstein Institute), Am Mühlenberg 1, Potsdam 14476, Germany*

[2]*Department of Physics, University of Maryland, College Park, Maryland 20742, USA*

(Received 9 April 2018; published 17 October 2018)

For the first time, we construct an inspiral-merger-ringdown waveform model within the effective-one-body formalism for spinning, nonprecessing binary black holes that includes gravitational modes beyond the dominant $(\ell, |m|) = (2, 2)$ mode, specifically $(\ell, |m|) = (2, 1), (3, 3), (4, 4), (5, 5)$. Our multipolar waveform model incorporates recent (resummed) post-Newtonian results for the inspiral and information from 157 numerical-relativity simulations, and 13 waveforms from black-hole perturbation theory for the (plunge-)merger and ringdown. We quantify the improvement in accuracy when including higher-order modes by computing the faithfulness of the waveform model against the numerical-relativity waveforms used to construct the model. We define the faithfulness as the match maximized over time, phase of arrival, gravitational-wave polarization and sky position of the waveform model, and averaged over binary orientation, gravitational-wave polarization and sky position of the numerical-relativity waveform. When the waveform model contains only the (2,2) mode, we find that the averaged faithfulness to numerical-relativity waveforms containing all modes with $\ell \leq 5$ ranges from 90% to 99.9% for binaries with total mass 20–200 $M_\odot$ (using the Advanced LIGO's design noise curve). By contrast, when the (2,1), (3,3), (4,4), (5,5) modes are also included in the model, the faithfulness improves to 99% for all but four configurations in the numerical-relativity catalog, for which the faithfulness is greater than 98.5%. Starting from the complete inspiral-merger-ringdown model, we develop also a (stand-alone) waveform model for the merger-ringdown signal, calibrated to numerical-relativity waveforms, which can be used to measure multiple quasi-normal modes. The multipolar waveform model can be extended to include spin-precessional effects, and will be employed in upcoming observing runs of Advanced LIGO and Virgo.

DOI: 10.1103/PhysRevD.98.084028

I. INTRODUCTION

The Advanced LIGO detectors [1] have reported, so far, the observation of five gravitational-wave (GW) signals from coalescing binary black holes (BBHs): GW150914 [2], GW151226 [3], GW170104 [4], GW170608 [5], GW170814 [6] (observed also by the Virgo detector [7]), and one GW signal from a coalescing binary neutron star (BNS) [8]. The modeled search for GWs from binary systems and the extraction of binary parameters, such as the masses and spins, are based on the matched-filtering technique [9–14], which requires accurate knowledge of the waveform of the incoming signal. During the first two observing runs (O1 and O2), the Advanced LIGO and Virgo modeled-search pipelines employed, for binary total masses below 4 $M_\odot$, templates [15] built within the post-Newtonian (PN) approach [16–19], and, for binary total masses in the range 4–200 $M_\odot$, templates developed using the effective-one-body (EOB) formalism calibrated to numerical-relativity (NR) simulations [20–27]. For parameter-estimation analyses [8,10,28,29] and tests of general relativity (GR) [30], PN [16–18], EOBNR [25,27,31,32] and also inspiral-merger-ringdown phenomenological (IMRPhenom) waveform models [33–35] were used.

The -2 spin-weighted spherical harmonics comprise a convenient basis into which one can decompose the two polarizations of GWs. The spinning, nonprecessing EOBNR waveform model [27] employed in searches and parameter-estimation studies during the O2 run (henceforth, `SEOBNRv4` model), only used the dominant $(\ell, |m|) = (2, 2)$ mode to build the gravitational polarizations. This approximation was accurate enough for detecting and inferring astrophysical information of the sources observed during O2 (and also O1), as discussed in Refs. [36–44].

Because of the expected increase in sensitivity during the third observing run (O3), which is planned to start in the Fall of 2018, some GW signals are expected to have much larger signal-to-noise ratio (SNR) with respect to the past, and may lie in regions of parameter space so far unexplored

*roberto.cotesta@aei.mpg.de

(e.g., more massive and/or higher mass-ratio systems than observed in O1 and O2). This poses an excellent opportunity to improve our knowledge of astrophysical and gravitational properties of the sources, but it also requires more accurate waveform models to be able to take full advantage of the discovery and inference potential. More accurate waveform models would be useful, as well, from the detection point of view to further increase the effective volume reached by the search, in particular for regions of the parameter space where the approximation of restricting to the (2,2) mode starts to degrade [37–39]. Following these motivations, we build here an improved version of the `SEOBNRv4` waveform model that includes the modes $(\ell, |m|) = (2,1), (3,3), (4,4), (5,5)$ beyond the dominant (2,2) mode (henceforth, `SEOBNRv4HM` model). Similar work was done for the nonspinning case for the EOBNR waveform model of Ref. [45] (henceforth, `EOBNRv2HM` model), and for the nonspinning and spinning, nonprecessing `IMRPhenom` models in Refs. [46,47].

In building the `SEOBNRv4HM` model we incorporate new informations from PN calculations [48,49], from NR simulations (produced with the (pseudo) Spectral Einstein code (SpEC) [50] of the Simulating eXtreme Spacetimes (SXS) project and the Einstein Toolkit code [51,52]), and also from merger-ringdown waveforms computed in BH perturbation theory solving the Teukolsky equation [53,54]. The NR waveforms are described in Refs. [27,50,55–60], and summarized in Appendix F. They were also employed to build the `SEOBNRv4` waveform model in Ref. [27] (see Sec. III therein). However, here, we do not use the BAM simulation `BAMq8s85s85` [61,62], because the higher-order modes are not available to us. Thus, for the same binary configuration, we produce a new NR simulation using the Einstein Toolkit code and extract higher-order modes (henceforth, `ET:AEI:0004`).

As by product of the `SEOBNRv4HM` model, we obtain a (stand-alone) merger-ringdown model [27,63–67], tuned to the NR and Teukolsky-equation waveforms, which can be employed to extract multiple quasi-normal modes from GW signals, and test general relativity [68–71].

The paper is organized as follows. In Sec. II we use the NR waveforms at our disposal to quantify the importance of higher harmonics in presence of spins. In Sec. III we determine, taking also into account the error in NR waveforms, which gravitational modes are crucial to achieve at least ∼99% accuracy. In Sec. IV we develop the multipolar EOB waveform model, and describe how to enhance its performance by including information from NR simulations and BH perturbation theory. We also highlight the construction and use of the multipolar (stand-alone) merger-ringdown model. In Sec. V we compare the newly developed `SEOBNRv4HM` model to 157 NR waveforms. In Sec. VI we summarize our main conclusions, and outline possible future work. Finally, in Appendices A–C we provide interested readers with explicit expressions of all quantities entering the higher-order modes of the `SEOBNRv4HM` model, and point out the presence of numerical artifacts in the (4,4) and (5,5) modes of some NR simulations. For convenience, we summarize in Appendix F the NR waveforms used in this paper. In Appendix G we also compare the model `SEOBNRv4HM` with the nonspinning `EOBNRv2HM` waveform model, developed in 2011 [45]. Finally in Appendix H we compare the `SEOBNRv4HM` model with an NR waveform in time domain.

In this paper we adopt the geometric units $G = c = 1$.

II. MOTIVATIONS TO MODEL HIGHER-ORDER MODES FOR BINARY BLACK HOLES

In this section we describe the spherical-mode decomposition of the gravitational polarizations and discuss the motivations for building an inspiral-merger-ringdown waveform model (`SEOBNRv4HM`) with higher harmonics for spinning BHs.

Henceforth, we denote the binary's total mass with $M = m_1 + m_2$, and choose the body's masses m_1 and m_2 such that the mass ratio $q = m_1/m_2 \geq 1$. Since we consider only spinning, nonprecessing BHs (i.e., spins aligned or antialigned with the direction perpendicular to the orbital plane $\hat{\mathbf{L}}$), we only have one (dimensionless) spin parameter for each BH, $\chi_{1,2}$, defined as $\mathbf{S}_{1,2} = \chi_{1,2} m_{1,2}^2 \hat{\mathbf{L}}$, where $\mathbf{S}_{1,2}$ are the BH's spins ($-1 \leq \chi_{1,2} \leq 1$).

The observer-frame's gravitational polarizations read

$$h_+(\iota, \varphi_0; t) - i h_\times(\iota, \varphi_0; t) = \sum_{\ell=2}^{\infty} \sum_{m=-\ell}^{\ell} {}_{-2}Y_{\ell m}(\iota, \varphi_0) h_{\ell m}(t), \tag{2.1}$$

where we denote with ι the inclination angle (computed with respect to the direction perpendicular to the orbital plane), φ_0 the azimuthal direction to the observer, and ${}_{-2}Y_{\ell m}(\iota, \varphi_0)$'s the -2 spin-weighted spherical harmonics. For spinning, nonprecessing BHs' we have $h_{\ell m} = (-1)^\ell h^*_{\ell -m}$. Thus, without loss of generality, we restrict the discussion to (ℓ, m) modes with $m > 0$.

As we shall discuss below, for face-on/face-off binary configurations, the dominant mode is the $(\ell, m) = (2,2)$ mode. For generic binary orientations the modes $(\ell, m) \neq (2,2)$ could be comparable to the (2,2) mode. Nevertheless, we will loosely refer to $(\ell, m) \neq (2,2)$ as subdominant modes; sometime we also refer to them as higher-order modes or higher harmonics, even if they include the (2,1) mode.

Several authors in the literature have investigated the impact of neglecting higher-order modes for detection and parameter estimation. From the detection perspective, Refs. [37,38,40,72] showed that neglecting higher-order modes in nonspinning gravitational waveforms can cause a

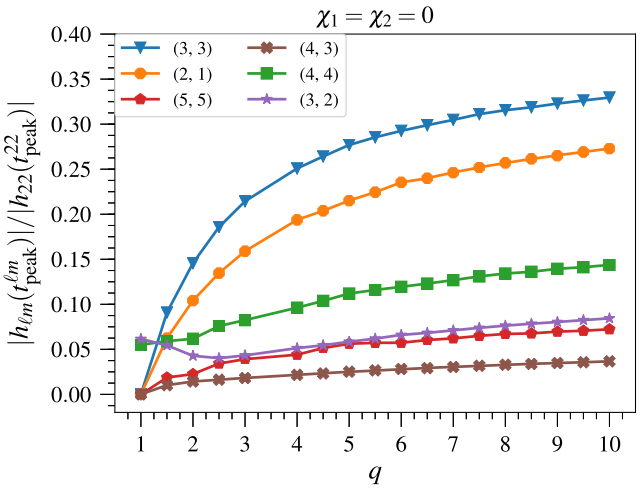

FIG. 1. Amplitude ratio between the (ℓ, m) mode and the dominant (2,2) mode, both evaluated at their peak, as function of the mass ratio. We use only nonspinning NR waveforms. (Note that the markers represent the NR data, and we connect them by a line). We note that the importance of a given higher-order mode with respect to the dominant one is not controlled only by the amplitude ratio between the two, but also by the -2 spin-weighted spherical harmonic associated to the mode [see Eq. (2.1)].

loss in detection volume bigger than 10% when the mass ratio $q \geq 4$ and total mass $M \geq 100\ M_\odot$. To overcome this issue, Ref. [39] suggested a new method to search for GW signals with templates that include higher modes, increasing the search sensitivity up to a factor of 2 in volume for high mass-ratio, and high total-mass binaries. While those works consider only nonspinning systems, the authors of Ref. [73] show that for spinning systems, the loss in detection volume due to neglecting higher-order modes is smaller with respect to the nonspinning case. This happens because the spin parameters provide an additional degree of freedom that templates with only the dominant (2,2) mode can employ to better match signals containing higher-order modes.

From the parameter-estimation perspective, as discussed in Ref. [40], for nonspinning systems with mass ratio $q \geq 4$ and total masses $M \geq 150\ M_\odot$ the systematic error due to neglecting higher-order modes is larger than the 1σ statistical error for signals with signal-to-noise ratio (SNR) of 8. Signals with a larger SNR yield smaller statistical errors and, the constraints discussed before become more stringent [36]. Indeed even for equal-mass systems, where the higher-order modes are expected to be negligible, if the signal has an SNR of 48, the systematic error from neglecting higher-order modes can be bigger than the statistical error [36]. (The SNRs above refer to Advanced LIGO's "zero-detuned high-power" design sensitivity curve [74]).

Here we briefly review known results, and highlight some features that will be exploited below when building the `SEOBNRv4HM` waveform model.

In Fig. 1 we show the ratio between the largest subdominant (ℓ, m) modes and the (2,2) mode amplitudes, evaluated at their peak, $t^{\ell m}_{\rm peak}$ and $t^{22}_{\rm peak}$, respectively, as function of mass ratio for all the nonspinning waveforms in our NR catalog. We note that the well-known mode hierarchy $(\ell, m) = (2,2), (3,3), (2,1), (4,4), (3,2), (5,5), (4,3)$ changes when approaching the equal-mass (equal-spin) limit (see, e.g., Ref. [75]). Indeed, in this limit all modes with odd m have to vanish in order to enforce the binary's symmetry under rotation $\varphi_0 \to \varphi_0 + \pi$. Thus, when $\nu \to 1/4$ ($\chi_1 = \chi_2$), the (3,2) and (4,4) modes become the most important subdominant modes. In Fig. 2 we show how the modes' hierarchy in the nonspinning case (see Fig. 1) changes when BH's spins are included. In particular, in the left panel of Fig. 2 we fix the mass ratio to $q = 8$ and plot the relative amplitude of the modes as function of the spin of the more massive BH. Note that for $q = 8$ all NR waveforms in our catalog (with the

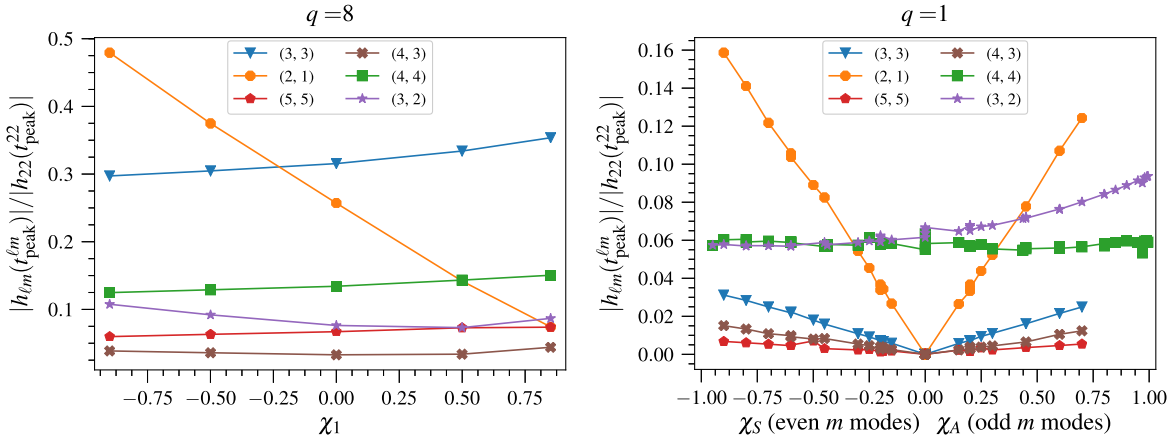

FIG. 2. Amplitude ratio between the (ℓ, m) mode and the dominant (2,2) mode, both evaluated at their peak. In the left (right) panel we plot these quantities for mass ratio $q = 8$ versus the spin of the heavier BH ($q = 1$ versus $\chi_A = (\chi_1 - \chi_2)/2$ for modes with odd m, and $\chi_S = (\chi_1 + \chi_2)/2$ for modes with even m). The markers represent the NR data, and we connect them by a line.

exception of `ET:AEI:0004`, $q=8, \chi_1=\chi_2=0.85$) have the spin only on the more massive BH. We see that the relative amplitude of the modes (3,3), (4,4), (3,2), (5,5), (4,3) depends weakly on the spins, except for the (2,1) mode. Indeed, for $\chi_1 \gtrsim 0.5$, the (2,1) mode becomes smaller than the (4,4) mode and for $\chi_1 \gtrsim 0.75$ is as small as the modes (3,2), (5,5). On the other side, for $\chi_1 \lesssim -0.25$ the mode (2,1) is larger than the (3,3) mode. We find that for smaller mass ratios the effect of χ_2 (i.e., the spin of the lighter BH), becomes more important. In particular, for a fixed value of χ_1 the amplitude ratio $|h_{\ell m}(t^{\ell m}_{\rm peak})|/|h_{22}(t^{22}_{\rm peak})|$ for the modes (3,3), (4,4), (5,5) decreases with increasing χ_2, while the ratio increases for the modes (2,1), (3,2), (4,3).

The special case of equal-mass systems, $q=1$, is discussed in the right panel of Fig. 2. Here we show the amplitude ratio between the (ℓ, m) mode and the dominant (2,2) mode, both evaluated at their peak, as function of $\chi_A=(\chi_1-\chi_2)/2$ for modes with odd m and as function of $\chi_S=(\chi_1+\chi_2)/2$ for modes with even m. As discussed before, the modes with odd m vanish for equal-mass, equal-spins configurations ($\chi_A=0$) from symmetry arguments and, the amplitude ratio grows proportionally to $|\chi_A|$ for these modes. In particular, we note that in this case the (2,1) mode behaves differently from the other modes, undergoing a much more significant growth in the amplitude ratio. Regarding the modes with even m, we notice that whereas the (4,4) mode is nearly constant as function of χ_S in the spin range considered, the (3,2) mode increases as a function of χ_S in the same range. The amplitude of the (2,1) mode has a stronger dependence on the spins with respect to the other modes because in its PN expansion the spin term enters at a lower relative order (see Eqs. (38a)–(38i) in Ref. [76]). A similar spin-dependence was found in Ref. [77] for the amplitudes ratio $(A_{\ell m}/A_{22})$ of the quasinormal mode oscillations.

Finally, it is worth emphasizing that in understanding the relevance of subdominant modes for the observer, it is important to take into account the -2 spin-weighted spherical-harmonic factor ${}_{-2}Y_{\ell m}(\iota,\varphi_0)$ that enters Eq. (2.1), notably its dependence on the angles (ι,φ_0). Indeed, the -2 spin-weighted spherical harmonic associated to the dominant mode starts from a maximum in the face-on orientation ($\iota=0$) and decreases to a minimum at edge-on ($\iota=\pi/2$). On the other hand, the spherical harmonics favor the higher-order modes with respect to the dominant one in orientations close to edge-on where $|{}_{-2}Y_{\ell m}(\iota\to\pi/2)|/|{}_{-2}Y_{22}(\iota\to\pi/2)|>1$. Furthermore, a direct inspection of the harmonic factor shows that the modes (3,2), (4,3) are suppressed (i.e., $|{}_{-2}Y_{\ell m}(\iota)|/|{}_{-2}Y_{22}(\iota)|<1$) for a larger region in ι than for the modes (3,3), (2,1), (4,4), (5,5). For this reason the contribution of the former to the gravitational polarizations is limited to a smaller number of orientations with respect to the latter.

III. SELECTING THE MOST-IMPORTANT HIGHER-ORDER MODES FOR MODELING

In this section we first introduce the faithfulness function as a tool to assess the closeness of two waveforms when higher-order modes are included. Then, we use it to estimate how many gravitational modes we need to model in order not to lose more than 10% in event rates when restricting to the binary's configurations in the NR catalog at our disposal. We also determine the loss in faithfulness of the NR waveforms due to numerical error.

The GW signal measured from a spinning, nonprecessing and noneccentric BBH is characterized by 11 parameters, namely the masses of the two bodies m_1 and m_2, the (constant) projection of the spins in the direction perpendicular to the orbital plane, χ_1 and χ_2, the angular position of the line of sight measured in the source's frame (ι,φ_0) [see Eq. (2.1)], the sky location of the source in the detector frame (θ,ϕ), the polarization angle ψ, the luminosity distance of the source $D_{\rm L}$ and the time of arrival $t_{\rm c}$. The signal measured by the detector takes the form:

$$h \equiv F_+(\theta,\phi,\psi)h_+(\iota,\varphi_0,D_{\rm L},\boldsymbol{\xi},t_{\rm c};t) + F_\times(\theta,\phi,\psi)h_\times(\iota,\varphi_0,D_{\rm L},\boldsymbol{\xi},t_{\rm c};t), \tag{3.1}$$

where for convenience we introduce $\boldsymbol{\xi}\equiv(m_1,m_2,\chi_1,\chi_2)$. The functions $F_+(\theta,\phi,\psi)$ and $F_\times(\theta,\phi,\psi)$ are the antenna patterns [15,78]:

$$F_+(\theta,\phi,\psi)=\frac{1+\cos^2(\theta)}{2}\cos(2\phi)\cos(2\psi)+ -\cos(\theta)\sin(2\phi)\sin(2\psi), \tag{3.2}$$

$$F_\times(\theta,\phi,\psi)=\frac{1+\cos^2(\theta)}{2}\cos(2\phi)\sin(2\psi) +\cos(\theta)\sin(2\phi)\cos(2\psi). \tag{3.3}$$

Equation (3.1) can be rewritten as:

$$h\equiv\mathcal{A}(\theta,\phi)[\cos\kappa(\theta,\phi,\psi)h_+(\iota,\varphi_0,D_{\rm L},\boldsymbol{\xi},t_{\rm c};t) +\sin\kappa(\theta,\phi,\psi)h_\times(\iota,\phi,D_{\rm L},\boldsymbol{\xi},t_{\rm c};t)], \tag{3.4}$$

where $\kappa(\theta,\phi,\psi)$ is the *effective polarization* [38] defined in the region $[0,2\pi)$ as:

$$e^{i\kappa(\theta,\phi,\psi)}=\frac{F_+(\theta,\phi,\psi)+iF_\times(\theta,\phi,\psi)}{\sqrt{F_+^2(\theta,\phi,\psi)+F_\times^2(\theta,\phi,\psi)}}, \tag{3.5}$$

while $\mathcal{A}(\theta,\phi)$ reads:

$$\mathcal{A}(\theta,\phi)=\sqrt{F_+^2(\theta,\phi,\psi)+F_\times^2(\theta,\phi,\psi)}. \tag{3.6}$$

We stress that $\mathcal{A}(\theta,\phi)$ does not depend on ψ despite the fact F_+ and $F_\times$ depend on it. Henceforth, to simplify the

notation we suppress the dependence of κ on (θ,ϕ,ψ). Given a GW signal $h_{\rm s}$ and a template waveform $h_{\rm t}$, we define the faithfulness as [38,79]

$$\mathcal{F}(\iota_{\rm s},\varphi_{0{\rm s}},\kappa_{\rm s}) \equiv \max_{t_c,\varphi_{0{\rm t}},\kappa_{\rm t}} \left[\frac{(h_{\rm s},h_{\rm t})}{\sqrt{(h_{\rm s},h_{\rm s})(h_{\rm t},h_{\rm t})}} \bigg|_{\substack{\iota_{\rm s}=\iota_{\rm t} \\ \xi_{\rm s}=\xi_{\rm t}}} \right], \tag{3.7}$$

where parameters with the subscript "s" ("t") refer to the signal (template) waveform. The inner product is defined as [15,78]:

$$(a,b) \equiv 4{\rm Re}\int_{f_{\rm l}}^{f_{\rm h}} df \frac{\tilde{a}(f)\tilde{b}^*(f)}{S_n(f)}, \tag{3.8}$$

where a tilde indicates the Fourier transform, a star the complex conjugate and $S_n(f)$ is the one-sided power spectral density (PSD) of the detector noise, and we employ the Advanced LIGO's "zero-detuned high-power" design sensitivity curve [74]. The integral is evaluated between the frequencies $f_{\rm l}=20$ Hz and $f_{\rm h}=3$ kHz. When the signal is an NR waveform that starts (ends) at a higher (lower) frequency than $f_{\rm l}$ ($f_{\rm h}$), we choose the starting (ending) frequency of the NR waveform. Note that the dependence on the luminosity distance $D_{\rm L}$ disappears in Eq. (3.7) because template and signal are normalized in that expression. In principle, we could define the faithfulness in Eq. (3.7) maximizing also over the inclination angle $\iota_{\rm t}$. This would certainly increase the faithfulness. However, as we have discussed in the previous section, the inclination angle ι affects considerably how higher-order modes impact the signal, thus we find more appropriate to investigate the waveform model in the worst situation in which we do not allow any bias in the measurement of the inclination angle.

The maximizations over t_c and $\varphi_{0{\rm t}}$ in Eq. (3.7) are computed numerically, while the maximization over $\kappa_{\rm t}$ is done analytically following the procedure described in Ref. [38] (see Appendix A). When $h_{\rm t}$ does not include higher-order modes, the maximization over the effective polarization $\kappa_{\rm t}$ in Eq. (3.7) becomes degenerate with the maximization over $\varphi_{0{\rm t}}$ and we recover the usual definition of faithfulness.

The faithfulness given in Eq. (3.7) depends on the signal parameters $(\iota_{\rm s},\varphi_{0{\rm s}},\kappa_{\rm s})$. To understand how the faithfulness varies as function of those parameters, we introduce the minimum, maximum, average and average weighted with the SNR unfaithfulness $[1-\mathcal{F}(\iota_{\rm s},\varphi_{0{\rm s}},\kappa_{\rm s})]$ over these parameters, namely [38,79,80]:

$$\min_{\iota_{\rm s},\varphi_{0{\rm s}},\kappa_{\rm s}} (1-\mathcal{F}) \equiv 1 - \max_{\iota_{\rm s},\varphi_{0{\rm s}},\kappa_{\rm s}} \mathcal{F}(\iota_{\rm s},\varphi_{0{\rm s}},\kappa_{\rm s}), \tag{3.9}$$

$$\max_{\iota_{\rm s},\varphi_{0{\rm s}},\kappa_{\rm s}} (1-\mathcal{F}) \equiv 1 - \min_{\iota_{\rm s},\varphi_{0{\rm s}},\kappa_{\rm s}} \mathcal{F}(\iota_{\rm s},\varphi_{0{\rm s}},\kappa_{\rm s}), \tag{3.10}$$

$$\langle 1-\mathcal{F}\rangle_{\iota_{\rm s},\varphi_{0{\rm s}},\kappa_{\rm s}} \equiv 1 - \frac{1}{8\pi^2}\int_0^{2\pi} d\kappa_{\rm s}\int_{-1}^{1} d(\cos\iota_s)\int_0^{2\pi} d\varphi_{0{\rm s}}\mathcal{F}(\iota_{\rm s},\varphi_{0{\rm s}},\kappa_{\rm s}), \tag{3.11}$$

$$\langle 1-\mathcal{F}\rangle^{\rm SNRweighted}_{\iota_{\rm s},\varphi_{0{\rm s}},\kappa_{\rm s}} \equiv 1 - \sqrt[3]{\frac{\int_0^{2\pi} d\kappa_{\rm s}\int_{-1}^{1} d(\cos\iota_s)\int_0^{2\pi} d\varphi_{0{\rm s}}\mathcal{F}^3(\iota_{\rm s},\varphi_{0{\rm s}},\kappa_{\rm s}){\rm SNR}^3(\iota_{\rm s},\varphi_{0{\rm s}},\kappa_{\rm s})}{\int_0^{2\pi} d\kappa_{\rm s}\int_{-1}^{1} d(\cos\iota_s)\int_0^{2\pi} d\varphi_{0{\rm s}}{\rm SNR}^3(\iota_{\rm s},\varphi_{0{\rm s}},\kappa_{\rm s})}}, \tag{3.12}$$

where the ${\rm SNR}(\iota_{\rm s},\varphi_{0{\rm s}},\theta_{\rm s},\phi_{\rm s},\kappa_{\rm s},D_{\rm Ls},\boldsymbol{\xi}_{\rm s},t_{c{\rm s}})$ is defined as:

$${\rm SNR}(\iota_{\rm s},\varphi_{0{\rm s}},\theta_{\rm s},\phi_{\rm s},\kappa_{\rm s},D_{\rm Ls},\boldsymbol{\xi}_{\rm s},t_{c{\rm s}}) \equiv \sqrt{(h_{\rm s},h_{\rm s})}. \tag{3.13}$$

We note that for the average unfaithfulness weighted with the SNR in Eq. (3.12), we drop in the SNR the explicit dependence on $\mathcal{A}(\theta,\phi)$ and $D_{\rm L}$, because they cancel out. It is important to highlight that the unfaithfulness weighted with the cube of the SNR is a conservative upper limit of the fraction of detection volume lost. Indeed, weighting the unfaithfulness with the SNR takes into account that, at a fixed distance, configurations closer to an edge-on orientation have a smaller SNR with respect to configurations closer to a face-on orientation, therefore they are less likely to be observed. The definitions of minimum, maximum and averaged unfaithfulness in Eqs. (3.9)–(3.11) are similar to those in Ref. [32], with the difference that in the latter they minimize, maximize and average also over the source orientation $\iota_{\rm s}$. The average weighted with the SNR in Eq. (3.12) was introduced in Ref. [80] and used for a similar purpose also in Ref. [79].

In the following we shall show results where all the averages are computed assuming an isotropic distribution for the source orientation and sky position.

Using the aforementioned definitions (3.9)–(3.12), we compute the unfaithfulness assuming that the signal is an NR waveform with modes $(\ell\leq 5, m\neq 0)$,[1] and the template is either an NR waveform or a `SEOBNRv4` waveform with only the (2,2) mode.

[1]Since the nonoscillating $m=0$ modes are not well reproduced by NR simulations and their contribution is small, we do not include them in these calculations. We find that the contribution of the modes with $\ell\geq 6$ is negligible.

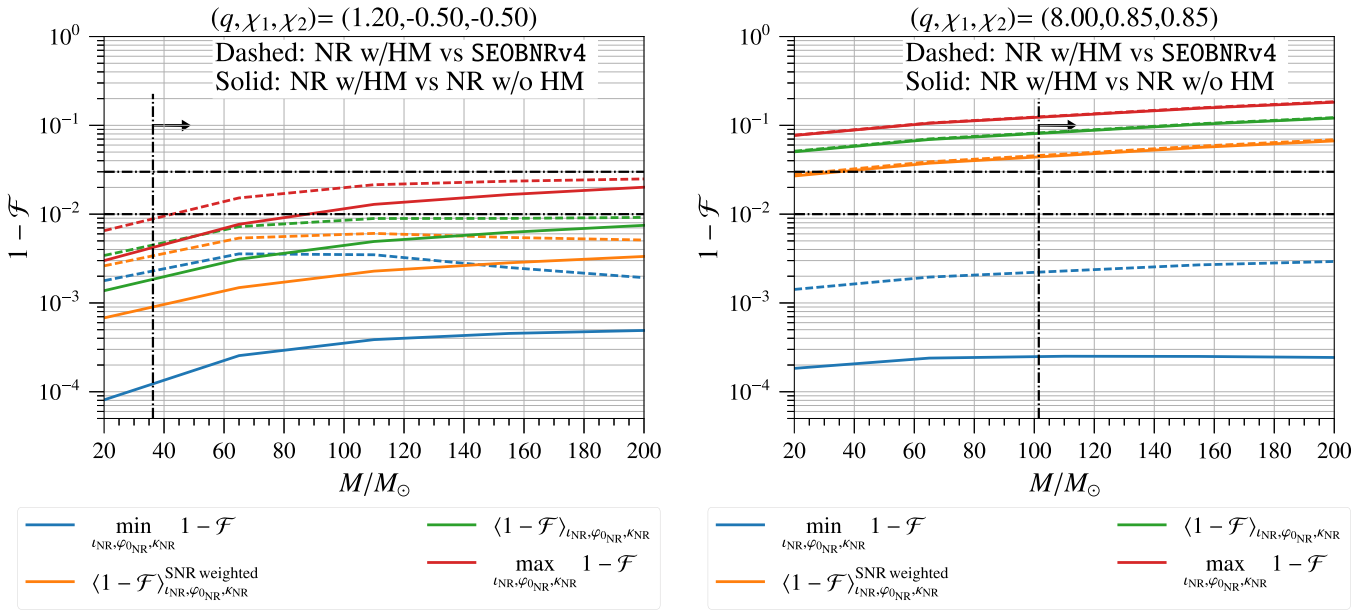

FIG. 3. Unfaithfulness $(1-\mathcal{F})$ for the configurations $(q=1.2,\chi_1=-0.5,\chi_2=-0.5)$ (left panel) and $(q=8,\chi_1=0.85,\chi_2=0.85)$ (right panel) in the mass range $20\,M_\odot \leq M \leq 200\,M_\odot$. In dashed the results for the SEOBNRv4 model and in solid the results for the NR waveform containing only the dominant mode, both against the NR waveform with the modes $(\ell \leq 5, m \neq 0)$. The minimum of the unfaithfulness (blue curves) correspond to a face-on orientation. We also show the unfaithfulness averaged over the three angles $\iota_{NR},\phi_{0NR},\kappa_{NR}$ (green curves) and weighted by the cube of the SNR (orange curves). Finally the minimum of the unfaithfulness (red curves) which in practice correspond to edge-on and minimized over the other two angles. The vertical dotted-dashed black line is the smallest mass for which the $(\ell,m)=(2,1)$ mode is entirely in the Advanced LIGO band. The $(\ell,|m'|)$ mode is entirely in the Advanced LIGO band starting from a mass m' times the mass associated with the $(\ell,m)=(2,1)$ mode. The horizontal dotted-dashed black lines represent the values of 1% and 3% unfaithfulness.

In the left panel of Fig. 3 we show results for the simulation SXS:BBH:0610 having $q=1.2,\chi_1=-0.5,\chi_2=-0.5$. Given the small mass ratio, we do not expect the higher-modes to play an important role. Indeed both the NR with only the dominant mode and the SEOBNRv4 model have averaged unfaithfulness $<1\%$ in the mass range $20\,M_\odot \leq M \leq 200\,M_\odot$. In both cases the unfaithfulness is maximum for an edge-on orientation and is $<3\%$. Conversely the minima of the unfaithfulness occur for a face-on configuration and they are always much smaller than 1%. The situation is very different in the right panel of Fig. 3 where we consider the simulation ET:AEI:0004 that has larger mass ratio and spins: $q=8,\chi_1=\chi_2=0.85$. In this case the minima of the unfaithfulness correspond to a face-on orientation where the higher-order modes are negligible and for this reason both NR with only the dominant mode and the SEOBNRv4 model have unfaithfulness smaller than 1%. By contrast, the results for the maximum of the unfaithfulness correspond to an edge-on orientation and they are equally large for the NR with only the dominant mode and for the SEOBNRv4 model. They have unfaithfulness in the range [10%, 20%] for masses $20\,M_\odot \leq M \leq 200\,M_\odot$. In this case also the averaged unfaithfulness are large, in the range [5%, 15%] and [3%, 8%] for the weighted averages.

Thus, for this high mass-ratio configuration the error from neglecting higher-order modes supersedes the modeling error of the dominant mode when the orientation is far from face-on/face-off. This is not surprising because the SEOBNRv4 waveform model was constructed requiring 1% of maximum unfaithfulness against the NR waveforms when only the (2,2) mode was included [27].

Only by properly including the largest subdominant modes can one hope to achieve an unfaithfulness of the waveform model below 1%.[2] Which subdominant modes should we include to achieve such an accuracy? To address this question, we compute the faithfulness between NR waveforms including the modes (2,2), (2,1), (3,3), (4,4), (5,5) and NR waveforms including only the $(\ell \leq 5, m \neq 0)$ modes. We find that the unfaithfulness averaged over the three angles $(\iota_{NR},\varphi_{0NR},\kappa_{NR})$ ranges between $0.01\% \lessapprox (1-\mathcal{F}) \lessapprox 0.5\%$ for the total mass interval $20\,M_\odot \leq M \leq 200\,M_\odot$. Thus, we conclude that the modes (2,2), (2,1), (3,3), (4,4), (5,5) are sufficient to model the full GW signal if we want to achieve an average unfaithfulness smaller than 1%. Furthermore, we note that these modes are not enough to ensure that the maximum of the unfaithfulness is smaller than 1%. In fact, for some of the configurations with higher mass ratio, the unfaithfulness is slightly larger

[2]We notice that using a waveform model with unfaithfulness smaller than 3% (or 1% depending on the features of the template bank) is a sufficient condition for a template bank to have a loss in event rates due to modeling error and discreteness of the template bank smaller than 10% (e.g., see Ref. [17]).

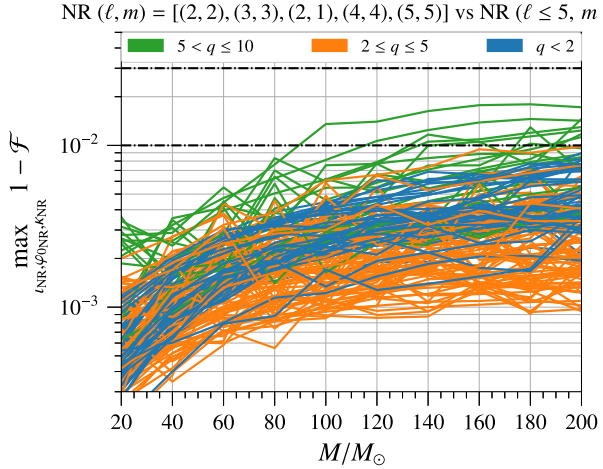

FIG. 4. Maximum of unfaithfulness $(1-\mathcal{F})$ over the three angles $(\iota_{\rm NR}, \varphi_{0\rm NR}, \kappa_{\rm NR})$ as a function of the total mass, in the range $20\ M_\odot \leq M \leq 200\ M_\odot$ of the NR waveform with (2,2), (2,1), (3,3), (4,4), (5,5) modes against NR waveform with $(\ell \leq 5, m \neq 0)$ modes. The maximum unfaithfulness is typically reached for edge-on orientations. The jaggedness of the curves is caused by the numerical noise present in higher-order modes that are less resolved in the NR simulations. We find that this feature is not present when these noisy modes are removed from the calculation of the faithfulness.

than 1% in the mass range $20\ M_\odot \leq M \leq 200\ M_\odot$, as it is clear from the plot in Fig. 4. The maximum unfaithfulness decreases, almost reaching the requirement of being below 1% for all the waveforms in the catalog, if we add also the more subdominant modes (3,2), (4,3). However, given that the overall improvement in the maximum of unfaithfulness when including also the modes (3,2), (4,3) is small (of the order of a few 0.1%) with respect to the results obtained using only the (2,2), (2,1), (3,3), (4,4), (5,5) modes, it is worth comparing this improvement with the estimation of the maximum of the unfaithfulness due to the numerical error of the NR waveforms. The numerical errors we consider are numerical truncation error [57,81] and waveform extrapolation error [57,81,82]. For our NR catalog, we estimate the numerical truncation error computing the maximum of the unfaithfulness between the same NR waveforms with the same modes [i.e., (2,2), (2,1), (3,3), (4,4), (5,5)], but with different resolutions, notably the highest (maximum) resolution and the second highest. The waveform extrapolation error is estimated in the same way, but employing different extrapolation orders (i.e., $N = 2$ and $N = 3$). We find that the contribution of each of these errors to the maximum of the unfaithfulness is in the range [0.1%, 1%] for the total mass interval $20\,M_\odot \leq M \leq 200\,M_\odot$.[3]

[3]The unfaithfulness averaged over the three angles $(\iota_{\rm NR}, \varphi_{0\rm NR}, \kappa_{\rm NR})$ due to numerical errors is much smaller than 1%. The reason is that the main contribution to this average unfaithfulness is the numerical error of the dominant mode. The latter is much smaller than 1%, as well. This conclusion is in agreement with Ref. [57] where the authors studied the numerical errors of the dominant mode for a subset of the waveforms in our NR catalog.

Since adding the modes (3,2), (4,3) is a non trivial task because of the mode mixing between spherical and spheroidal harmonics [65,83–85], and considering that their contribution is at the same level of the numerical error of the NR waveforms, we decide not to include them in the SEOBNRv4HM model. The results of the maximum of the unfaithfulness due to the numerical errors suggest that in order to use NR waveforms to build an EOBNR model having maximum unfaithfulness against NR smaller than 1% it would be necessary to have more accurate higher-order modes from NR simulations.

IV. EFFECTIVE-ONE-BODY MULTIPOLAR WAVEFORMS FOR NONPRECESSING BINARY BLACK HOLES

In this section we describe the main ingredients used to build the multipolar spinning, nonprecessing SEOBNRv4HM waveform model. We start briefly describing the dynamics in Sec. IV A, and then focus on the structure of the gravitational modes in Sec. IV B.

In the EOB formalism the real dynamics of two bodies with masses $m_{1,2}$ and spins $\mathbf{S}_{1,2}$ is mapped into the effective dynamics of a test particle with mass μ and spin $\mathbf{S}_*$ moving in a deformed Kerr metric with mass $M = m_1 + m_2$ and spin $\boldsymbol{S}_{\rm Kerr}$ (for details see Ref. [86]). As discussed above, here we limit to nonprecessing spins $\mathbf{S}_{1,2}$ and introduce the dimensionless spin parameters $\chi_{1,2}$ defined as $\mathbf{S}_{\rm i} = \chi_{\rm i} m_{\rm i}^2 \hat{\mathbf{L}}$, with $-1 \leq \chi_i \leq 1$.

A. Effective-one-body dynamics

The EOB conservative orbital dynamics is obtained from the resummed EOB Hamiltonian through the energy mapping [20]

$$H_{\rm EOB} = M\sqrt{1 + 2\nu\left(\frac{H_{\rm eff}}{\mu} - 1\right)}, \tag{4.1}$$

where $\mu = m_1 m_2/(m_1 + m_2)$ is the reduced mass of the BBH and $\nu = \mu/M$ is the symmetric mass ratio. When spins are nonprecessing the motion is constrained to a plane. Thus, the dynamical variables entering the Hamiltonian are the orbital phase ϕ,[4] the radial separation r (normalized to M) and their conjugate momenta p_ϕ and p_r (normalized to μ). The explicit form of $H_{\rm eff}$ that we adopt here was derived in Refs. [24,86], based on the linear-in-spin Hamiltonian for spinning test particles of Ref. [87]. The radial potential entering the 00-component of the EOB deformed metric, which also enters the effective Hamiltonian $H_{\rm eff}$, is explicitly given in Eqs. (2.2) and

[4]Abusing notation, we indicate the orbital phase with ϕ, which we use to denote the azimuthal angle describing the sky location of the source in the detector frame. It will be clear from the context which of the two angles we refer to.

(2.3) in Ref. [27]. The Hamiltonian $H_{\rm eff}$ depends also on the calibration parameters (K, $d_{\rm SO}$, $d_{\rm SS}$ $\Delta^{22}_{\rm peak}$), which were determined in Ref. [27] by requiring agreement against a large set of NR simulations (see Eqs. (4.12)–(4.15) therein). Here, we adopt the same values for these calibration parameters.

The dissipative dynamics in the EOB formalism is described by the radiation-reaction force given in Eq. (2.9) in Ref. [27]. We notice that in this paper we do not change the dissipative and conservative dynamics of the SEOBNRv4 model, and that the SEOBNRv4HM waveform models share the same two-body dynamics of SEOBNRv4. Here, we improve the accuracy of the gravitational modes with $(\ell, m) \neq (2, 2)$, and use them in the gravitational waveform, but we do not employ these more accurate version of the modes in the radiation-reaction force. Furthermore, we note that the gravitational modes with $(\ell, m) \neq (2, 2)$ are present in the radiation-reaction force, but they do not include the NQCs corrections [see Eq. (4.13)]. As discussed also in Ref. [45], the latter modify the amplitude of the already subdominant higher-order modes (see Fig. 1) by ∼10% close to merger, where the effect of the radiation reaction is not very important for the plunging dynamics.

B. Effective-one-body gravitational modes

As usual in the EOB formalism [21], the gravitational modes entering Eq. (2.1) are composed of two main parts: inspiral and plunge, and merger and ringdown. We can write the generic mode as:

$$h_{\ell m}(t) = \begin{cases} h^{\text{insp-plunge}}_{\ell m}(t), & t < t^{\ell m}_{\rm match} \\ h^{\text{merger-RD}}_{\ell m}(t), & t > t^{\ell m}_{\rm match}, \end{cases} \tag{4.2}$$

where $t^{\ell m}_{\rm match}$ is defined as:

$$t^{\ell m}_{\rm match} = \begin{cases} t^{22}_{\rm peak}, & (\ell, m) = (2,2), (3,3), (2,1), (4,4) \\ t^{22}_{\rm peak} - 10M, & (\ell, m) = (5,5), \end{cases} \tag{4.3}$$

with $t^{22}_{\rm peak}$ being the peak of the amplitude of the (2,2) mode. By construction the amplitude and phase of $h_{\ell m}(t)$ are C^1 at $t = t^{\ell m}_{\rm match}$. In the following we shall discuss in more detail how these two parts of the gravitational modes are built and why we choose a different matching point for the mode (5,5). We note again that the mode (2,2) in the SEOBNRv4HM model is the same as in the SEOBNRv4 model, and for this reason below we focus on the higher-order modes (3,3), (2,1), (4,4), (5,5).

C. Effective-one-body waveform modes: Inspiral-plunge

The inspiral-plunge EOB modes are expressed in the following multiplicative form:

$$h^{\text{insp-plunge}}_{\ell m} = h^{\rm F}_{\ell m} N_{\ell m}, \tag{4.4}$$

where $h^{\rm F}_{\ell m}$ is the factorized form of the PN GW modes [16,88] for quasicircular orbits, aimed at capturing strong-field effects, as discussed in the test-mass limit [76,89,90]. The factor $N_{\ell m}$ in Eq. (4.4) is the nonquasicircular (NQC) term, which includes possible radial effects that are no longer negligible during the late inspiral and plunge, and that are not captured by the rest of the waveform. More explicitly, the factorized term reads:

$$h^{\rm F}_{\ell m} = h^{(N,\epsilon)}_{\ell m} \hat{S}^{(\epsilon)}_{\rm eff} T_{\ell m} f_{\ell m} e^{i\delta_{\ell m}}, \tag{4.5}$$

where ϵ is the parity of the multipolar waveform, defined as

$$\epsilon = \begin{cases} 0, & \ell + m \text{ is even} \\ 1, & \ell + m \text{ is odd.} \end{cases} \tag{4.6}$$

The Newtonian term $h^{(N,\epsilon)}_{\ell m}$ reads:

$$h^{(N,\epsilon)}_{\ell m} = \frac{M\nu}{\rm D_L} n^{(\epsilon)}_{\ell m} c_{\ell+\epsilon}(\nu) V^{\ell}_{\phi} Y^{\ell-\epsilon,-m}\left(\frac{\pi}{2}, \phi\right), \tag{4.7}$$

where $\rm D_L$ is the distance from the source, $Y^{\ell m}(\theta, \phi)$ are the scalar spherical harmonics and the expression of the functions $n^{(\epsilon)}_{\ell m}$ and $c_{\ell+\epsilon}(\nu)$ are given in Appendix A. The function V^{ℓ}_{ϕ} is defined as:

$$V^{\ell}_{\phi} \equiv v^{(\ell+\epsilon)}_{\phi} \equiv M\Omega r_{\Omega}, \tag{4.8}$$

where

$$r_{\Omega} = \left[\frac{\partial H_{\rm EOB}(r, \phi, p_r = 0, p_{\phi})}{\partial p_{\phi}}\right]^{-\frac{2}{3}}, \tag{4.9}$$

$\Omega = d\phi/dt$ being the angular frequency. We also define $v_{\Omega} = (M\Omega)^{1/3}$. The term $\hat{S}^{(\epsilon)}_{\rm eff}$ in Eq. (4.5) is an effective source term:

$$\hat{S}^{(\epsilon)}_{\rm eff} = \begin{cases} H_{\rm eff}(r, p_{r_*}, p_{\phi}), & \epsilon = 0 \\ L_{\rm eff} = p_{\phi}(M\Omega)^{\frac{1}{3}}, & \epsilon = 1. \end{cases} \tag{4.10}$$

The function $T_{\ell m}$ in (4.5) is a resummation of the leading-order logarithms of tail effects:

$$T_{\ell m} = \frac{\Gamma(\ell+1-2iH_{\rm EOB}\Omega)}{\Gamma(\ell+1)}\exp[\pi m\Omega H_{\rm EOB}] \times \exp[2im\Omega H_{\rm EOB}\log(2m\Omega r_0)], \quad (4.11)$$

where $r_0 = 2M/\sqrt{e}$.

The functions $f_{\ell m}$ and $e^{\delta_{\ell m}}$ in Eq. (4.5) contain terms such that when expanding in PN order $h^{\rm F}_{\ell m}$ one recovers $h^{\rm PN}_{\ell m}$ (i.e., the PN expansion of the (ℓ, m) mode up to the PN order at which $h^{\rm PN}_{\ell m}$ is known today). In the SEOBNRv4HM model the expression for $f_{\ell m}$ and $\delta_{\ell m}$ are mostly taken from the SEOBNRv4 model [27] with the addition of some newly computed PN terms (for more details and explicit expressions of $f_{\ell m}$ and $\delta_{\ell m}$ see Appendix A). For the modes (2,1) and (5,5), $f_{\ell m}$ includes also the calibration term $c_{\ell m}\, v_\Omega^{\beta_{\ell m}}$, where $\beta_{\ell m}$ denotes the first-order term at which the PN series of $h_{\ell m}$ is not known today with its complete dependence on mass ratio and spins [see Eqs. (A11) and (A12)]. The calibration parameter $c_{\ell m}$ is evaluated to satisfy the condition:

$$|h^F_{\ell m}(t^{\ell m}_{\rm match})| \equiv |h^{(N,\epsilon)}_{\ell m}\hat{S}^{(\epsilon)}_{\rm eff} T_{\ell m} e^{i\delta_{\ell m}} f_{\ell m}(c_{\ell m})|_{t=t^{\ell m}_{\rm match}}, = |h^{\rm NR}_{\ell m}(t^{\ell m}_{\rm match})|, \quad \text{for } (\ell, m) = (2,1),(5,5), \quad (4.12)$$

where $|h^{\rm NR}_{\ell m}(t^{\ell m}_{\rm match})|$ is the amplitude of the NR modes at the matching point $t^{\ell m}_{\rm match}$. The latter are given as fitting formulas for every point of the parameter space (ν, χ_1, χ_2) in Appendix B. We need to include the calibration parameter $c_{\ell m}$ for the modes $(\ell, m) = (2,1),(5,5)$ for reasons that we explain below in Sec. IV D.

Finally, the term $N_{\ell m}$ in Eq. (4.4) is the NQC correction:

$$N_{\ell m} = \left[1 + \frac{p^2_{r^*}}{(r\Omega)^2}\left(a_1^{h_{\ell m}} + \frac{a_2^{h_{\ell m}}}{r} + \frac{a_3^{h_{\ell m}}}{r^{3/2}}\right)\right] \times \exp\left[i\left(b_1^{h_{\ell m}}\frac{p_{r^*}}{r\Omega} + b_2^{h_{\ell m}}\frac{p^3_{r^*}}{r\Omega}\right)\right], \quad (4.13)$$

which is used to reproduce the shape of the NR modes close to the matching point $t^{\rm match}_{\ell m}$. As done in the past [25,27], the 5 constants $(a_1^{h_{\ell m}}, a_2^{h_{\ell m}}, a_3^{h_{\ell m}}, b_1^{h_{\ell m}}, b_2^{h_{\ell m}})$ are fixed by requiring that:

(i) The amplitude of the EOB modes is the same as that of the NR modes at the matching point $t^{\ell m}_{\rm match}$:

$$|h^{\rm insp\text{-}plunge}_{\ell m}(t^{\ell m}_{\rm match})| = |h^{\rm NR}_{\ell m}(t^{\ell m}_{\rm match})|; \quad (4.14)$$

We notice that this condition is different from that in Eq. (4.12) because it affects $h^{\rm insp\text{-}plunge}_{\ell m}(t^{\ell m}_{\rm match})$ and not $h^{\rm F}_{\ell m}(t^{\ell m}_{\rm match})$.

(ii) The first derivative of the amplitude of the EOB modes is the same as that of the NR modes at the matching point $t^{\ell m}_{\rm match}$:

$$\left.\frac{d|h^{\rm insp\text{-}plunge}_{\ell m}(t)|}{dt}\right|_{t=t^{\ell m}_{\rm match}} = \left.\frac{d|h^{\rm NR}_{\ell m}(t)|}{dt}\right|_{t=t^{\ell m}_{\rm match}}; \quad (4.15)$$

(iii) The second derivative of the amplitude of the EOB modes is the same as that of the NR modes at the matching point $t^{\ell m}_{\rm match}$:

$$\left.\frac{d^2|h^{\rm insp\text{-}plunge}_{\ell m}(t)|}{dt^2}\right|_{t=t^{\ell m}_{\rm match}} = \left.\frac{d^2|h^{\rm NR}_{\ell m}(t)|}{dt^2}\right|_{t=t^{\ell m}_{\rm match}}; \quad (4.16)$$

(iv) The frequency of the EOB modes is the same as that of the NR modes at the matching point $t^{\ell m}_{\rm match}$:

$$\omega^{\rm insp\text{-}plunge}_{\ell m}(t^{\ell m}_{\rm match}) = \omega^{\rm NR}_{\ell m}(t^{\ell m}_{\rm match}); \quad (4.17)$$

(v) The first derivative of the frequency of the EOB modes is the same as that of the NR modes at the matching point $t^{\ell m}_{\rm match}$:

$$\left.\frac{d\omega^{\rm insp\text{-}plunge}_{\ell m}(t)}{dt}\right|_{t=t^{\ell m}_{\rm match}} = \left.\frac{d\omega^{\rm NR}_{\ell m}(t)}{dt}\right|_{t=t^{\ell m}_{\rm match}}, \quad (4.18)$$

where the RHS of Eqs. (4.14)–(4.18) (usually called "input values"), are given as fitting formulas for every point of the parameter space (ν, χ_1, χ_2) in Appendix B. These fits are produced using the NR catalog and BH-perturbation-theory waveforms, as described in Appendix F.

As we discuss in Appendices B and C, we find that for several binary configurations in the NR catalog, the numerical error is quite large for the mode (5,5) close to merger. To minimize the impact of the numerical error on the fits of the input values, we are obliged to choose the matching point for this mode earlier than for other modes, as indicated in Eq. (4.3).

D. Minima in (2,1), (5,5)-modes' amplitude and $c_{\ell m}$'s calibration parameters

We want now to come back to the motivation of introducing the $c_{\ell m}$'s calibration parameters in Eq. (4.12) for the modes (2,1) and (5,5). We note that those parameters are determined and included in the waveform before applying the NQC conditions (4.14)–(4.18). We introduce the $c_{\ell m}$'s to "cure" the behaviour of the modes (2,1), (5,5) close to the matching point for a particular region of the parameter space. Indeed, we find that the factorized expression of the amplitude $|h^{\rm F}_{\ell m}(t)|$ starts to decrease toward plunge and merger, approaching minimum values close to zero for $t \sim t^{\rm match}_{\ell m}$ when the binary parameters have $q \sim 1$ and large $|\chi_A| = |(\chi_1 - \chi_2)|/2$. Although the term $f_{\ell m}$ in

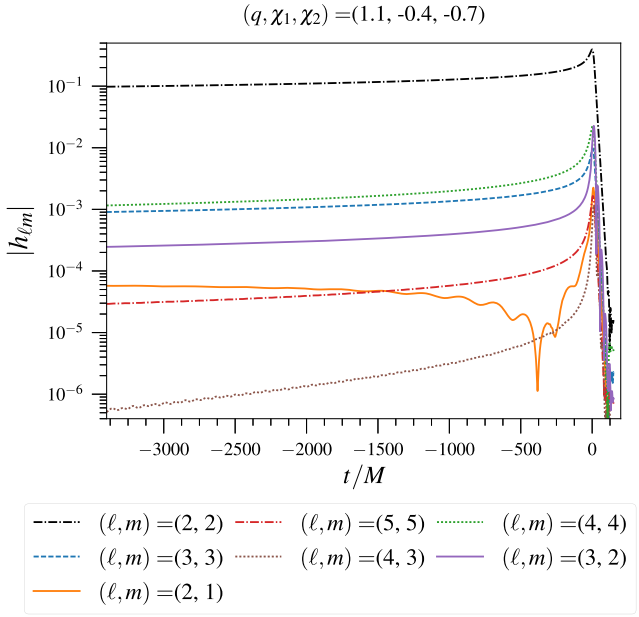

FIG. 5. Amplitude of the (2,2), (2,1), (3,3), (4,4), (5,5), (3,2), (4,3) modes versus time for the NR simulation `SXS:BBH:1377` with parameters $q = 1.1, \chi_1 = -0.4, \chi_2 = -0.7$. We produce such simulation to check if the analytical prediction that the (2,1)-mode's amplitude would have a nonmonotonic behavior toward merger holds. We choose as origin of time the peak of the (2,2) mode.

Eq. (4.5) is responsible of the zeros in the amplitude, we find that this unexpected behaviour is also present in the PN-expanded form of the mode, and persist in other mode resummations, like those suggested in Ref. [76] [see Eq. (2) therein] and in Refs. [91,92].

Quite interestingly, in the case of the (5,5) mode, we do not find such a nonmonotonic behavior toward merger in the NR simulations at our disposal, but we do find it for the (2,1) mode in the same region of parameter space predicted by the analytical computation. In particular, we notice minima toward merger in `SXS:BBH:0612` with $(q=1.6, \chi_1 = 0.5, \chi_2 = -0.5)$, `SXS:SXS:BBH:0614` $(q = 2, \chi_1 = 0.75, \chi_2 = -0.5)$, `SXS:BBH:0254` $(q = 2, \chi_1 = 0.6, \chi_2 = -0.6)$. We also produce a new NR simulation `SXS:BBH:1377` with $q = 1.1, \chi_1 = -0.4, \chi_2 = -0.7$ to check the presence of a minimum in the amplitude mode. Figure 5 shows indeed the presence of such a minimum in the (2,1) mode amplitude for `SXS:BBH:1377`.

The minima (or zeros) of the (2,1), (5,5) modes can sometime occur at times $t \sim t^{\rm match}_{\ell m}$, that is close to the times where we impose the NQC conditions (4.14)–(4.18). When that happens, the enforcement of such conditions yield a waveform which contains unwanted features.[5] Considering that for the mode (5,5) the minima are absent in the NR simulations, thus they are likely an artefact of the analytical waveform, and that for the mode (2,1) the minima are present only in the region of parameter space where the (2,1) mode is much smaller than the other modes (i.e., when $q \sim 1$ and $|\chi_A| = |(\chi_1 - \chi_2)|/2$ is large, see also Fig. 5), we decide to remove the minima from the (2,1) and (5,5) EOB modes. We achieve this by introducing the calibration parameter $c_{\ell m}$, which enforces the condition that the EOB amplitude at $t^{\rm match}_{\ell m}$ is equal to the NR amplitude [see Eq. (4.12)]. Note that the latter is imposed before the NQC conditions and removes the minima only when they appear for $t \sim t^{\ell m}_{\rm match}$. Modeling the minima in the (2,1) modes could be considered in the future, when more accurate waveforms would be needed at higher SNRs.

Henceforth, we attempt to describe why the analytical modes (both in the PN and factorized form) present minima or zeros for the (2,1) and (5,5) cases when $q \sim 1$ and $|\chi_A| = |(\chi_1 - \chi_2)|/2$ is large. Readers who might not be interested in this technical discussion, could skip the rest of this section and move to Sec. IV E.

As discussed in Sec. II, because of binary symmetry under rotation ($\varphi_0 \to \varphi_0 + \pi$) the modes with odd m vanish for equal-mass and equal-spins configurations. Thus, the nonspinning terms in those modes are proportional to $\delta m = (m_1 - m_2)/M$ while the spinning terms are an antisymmetric combination of δm, χ_A and $\chi_S = (\chi_1 + \chi_2)/2$ (e.g., $\chi_A, \chi_S \delta m, \chi_A^2 \delta m$), see e.g., Eqs. (38a)–(38i) in Ref. [76]. In the limit $q \sim 1$ all the nonspinning and spinning terms proportional to δm are suppressed, and the leading spinning terms are proportional to χ_A. For large values of χ_A and small values of δm (very unequal spins, almost equal mass) a cancellation between the leading-order spin correction and the dominant nonspinning PN term (which despite being of lower PN order is suppressed by δm) can occur at some given frequency. The higher the difference in PN orders between these two leading spinning and nonspinning contributions, the higher the frequency at which the cancellation happens. For the (2,1) mode, there is only a half PN order difference between these terms (see Eq. (38b) in Ref. [76]), so the cancellation arises at sufficiently low frequencies where this PN analysis based on two leading terms can be reliable, and, indeed, we do observe these minima in the NR simulations. In Table I we list the configurations in our NR catalog where the minimum happens and its orbital frequency as measured in the NR simulation[6] and as predicted by PN modeling at 3PN order [19,48,88]. As expected, the lower the frequency, the more accurate the PN prediction. We note that the last row shows results of a NR simulation that we specifically produce to confirm the presence of the minimum in the mode (see also Fig. 5). We note that for the binary's configuration listed in

[5]Since $|h^{\rm insp\text{-}plunge}_{\ell m}(t^{\ell m}_{\rm match})| \sim 0$, imposing the condition in Eq. (4.14) with $|h^{\rm NR}_{\ell m}(t^{\ell m}_{\rm match})| \neq 0$ forces the function $|N_{\ell m}|$, hence the amplitude $|h^{\rm insp\text{-}plunge}_{\ell m}(t)|$, to assume unphysically large values for $t < t^{\ell m}_{\rm match}$.

[6]We estimate the orbital frequency in the NR simulation as half of the gravitational frequency of the (2,2) mode.

TABLE I. For each NR simulation, binary's parameters and values of the orbital frequencies $M\Omega_0^{\rm NR}$ and $M\Omega_0^{\rm PN}$ at which the minimum of the (2,1) mode occurs.

NR name	q	χ_1	χ_2	$M\Omega_0^{\rm NR}$	$M\Omega_0^{\rm PN}$
SXS:BBH:0254	2	0.6	−0.6	0.17	n/a
SXS:BBH:0614	2	0.75	−0.5	0.082	0.057
SXS:BBH:0612	1.6	0.5	−0.5	0.068	0.047
SXS:BBH:1377	1.1	−0.4	−0.7	0.033	0.029

the first row of Table I, the NR simulation shows a high-frequency minimum, which is not reproduced by PN calculations, confirming that this analysis becomes less reliable in the high-frequency regime.

Lastly, as already pointed out above, for the (5,5) mode we do not observe any minimum in the NR simulations at our disposal. The most likely explanation is that the cancellation of the leading terms happens at frequencies high enough that the higher-order PN corrections would change the result (i.e., they completely remove the minimum or push it at frequency higher than the merger frequency).

E. Effective-one-body waveform modes: Merger-ringdown

We build the merger-ringdown EOB waveforms following Refs. [27,63,64,66], notably the implementation in Ref. [27]. The merger-ringdown mode reads:

$$h_{\ell m}^{\rm merger\text{-}RD}(t) = \nu \tilde{A}_{\ell m}(t) e^{i\tilde{\phi}_{\ell m}(t)} e^{-i\sigma_{\ell m 0}(t-t^{\ell m}_{\rm match})}, \tag{4.19}$$

where $\sigma_{\ell m 0}$ is the (complex) frequency of the least-damped QNM of the final BH. We denote $\sigma^{\rm R}_{\ell m} \equiv \Re(\sigma_{\ell m 0}) < 0$ and $\sigma^{\rm I}_{\ell m} \equiv -\Re(\sigma_{\ell m 0})$. For each mode (ℓ, m), we employ the frequency values tabulated in Refs. [69,93] as functions of the BH's mass and spin. We compute the remnant-BH's mass using the same fitting formula in Ref. [25], which is based on the phenomenological formula in Ref. [94], but we replace its equal-mass limit (see Eq. (11) in Ref. [94]) with the fit in Ref. [95] (see Eq. (9) of Ref. [95]). The remnant-BH's spin is computed using the spin formula in Ref. [96] (see Eq. (7) in Ref. [96]).

For the two functions $\tilde{A}_{\ell m}(t)$ and $\tilde{\phi}_{\ell m}(t)$, we use the ansätze [27]:

$$\tilde{A}_{\ell m}(t) = c^{\ell m}_{1,c} \tanh[c^{\ell m}_{1,f}(t - t^{\ell m}_{\rm match}) + c^{\ell m}_{2,f}] + c^{\ell m}_{2,c}, \tag{4.20}$$

$$\tilde{\phi}_{\ell m}(t) = \phi^{\ell m}_{\rm match} - d^{\ell m}_{1,c} \log\left[\frac{1 + d^{\ell m}_{2,f} e^{-d^{\ell m}_{1,f}(t-t^{\ell m}_{\rm match})}}{1 + d^{\ell m}_{2,f}}\right], \tag{4.21}$$

where $\phi^{\ell m}_{\rm match}$ is the phase of the inspiral-plunge mode (ℓ, m) at $t = t^{\ell m}_{\rm match}$. The coefficients $d^{\ell m}_{1,c}$ and $c^{\ell m}_{i,c}$[7] with $i = 1, 2$ are fixed by imposing that the functions $\tilde{A}_{\ell m}(t)$ and $\tilde{\phi}_{\ell m}(t)$ in Eq. (4.2) are of class C^1 at $t = t^{\ell m}_{\rm match}$. Those constraints allow us to express $c^{\ell m}_{i,c}$ in terms of $c^{\ell m}_{1,f}, c^{\ell m}_{2,f}, \sigma^{\rm R}_{\ell m}, |h^{\rm insp\text{-}plunge}_{\ell m}(t^{\ell m}_{\rm match})|, \partial_t |h^{\rm insp\text{-}plunge}_{\ell m}(t^{\ell m}_{\rm match})|$ as

$$c^{\ell m}_{1,c} = \frac{1}{c^{\ell m}_{1,f}\nu}[\partial_t |h^{\rm insp\text{-}plunge}_{\ell m}(t^{\ell m}_{\rm match})| - \sigma^{\rm R}_{\ell m} |h^{\rm insp\text{-}plunge}_{\ell m}(t^{\ell m}_{\rm match})|]\cosh^2(c^{\ell m}_{2,f}), \tag{4.22}$$

$$c^{\ell m}_{2,c} = -\frac{|h^{\rm insp\text{-}plunge}_{\ell m}(t^{\ell m}_{\rm match})|}{\nu} + \frac{1}{c^{\ell m}_{1,f}\nu}[\partial_t |h^{\rm insp\text{-}plunge}_{\ell m}(t^{\ell m}_{\rm match})| - \sigma^{\rm R}_{\ell m} |h^{\rm insp\text{-}plunge}_{\ell m}(t^{\ell m}_{\rm match})|] \cosh(c^{\ell m}_{2,f}) \sinh(c^{\ell m}_{2,f}), \tag{4.23}$$

and $d^{\ell m}_{1,c}$ in terms of $d^{\ell m}_{1,f}, d^{\ell m}_{2,f}, \sigma^{\rm I}_{\ell m}, \omega^{\rm insp\text{-}plunge}_{\ell m}(t^{\ell m}_{\rm match})$ as

$$d^{\ell m}_{1,c} = [\omega^{\rm insp\text{-}plunge}_{\ell m}(t^{\ell m}_{\rm match}) - \sigma^{\rm I}_{\ell m}] \frac{1 + d^{\ell m}_{2,f}}{d^{\ell m}_{1,f} d^{\ell m}_{2,f}}. \tag{4.24}$$

Let us emphasize again that the values of $|h^{\rm insp\text{-}plunge}_{\ell m}(t^{\ell m}_{\rm match})|$, $\partial_t |h^{\rm insp\text{-}plunge}_{\ell m}(t^{\ell m}_{\rm match})|$ and $\omega^{\rm insp\text{-}plunge}_{\ell m}(t^{\ell m}_{\rm match})$ are fixed by the NQCs conditions in Eqs. (4.14), (4.15), and (4.17) to be the same as the NR values $|h^{\rm NR}_{\ell m}(t^{\ell m}_{\rm match})|, \partial_t |h^{\rm NR}_{\ell m}(t^{\ell m}_{\rm match})|$ and $\omega^{\rm insp\text{-}plunge}_{\ell m}(t^{\ell m}_{\rm match})$ which are given in Appendix B as function of ν and a combination of the spins χ_1 and χ_2. Thus, we are left with only two free parameters in the amplitude $c^{\ell m}_{i,f}$ and in the phase $d^{\ell m}_{i,f}$. To obtain those parameters we first extract them applying a least-square fit in each point of the parameter space (ν, χ_1, χ_2) for which we have NR and Teukolsky-equation–based waveforms. Then, we interpolate those values in the rest of the parameter space using polynomial fits in ν and a combination of χ_1 and χ_2, as given explicitly in Appendix C.

Regarding the accuracy of our merger-ringdown model, for the modes (2,1) and (3,3) the average fractional difference in the amplitude between the model and the NR waveform is of the order of percent, while the average phase difference is $\lesssim$0.1 radians. For the modes (4,4) and (5,5) we are unable to determine a similar average error, because those modes are affected by numerical error at merger and during ringdown, as we discuss in Appendix C. We find that the average fractional difference in the amplitude (phase) between the model and the NR simulation can be in some cases on the order of 10% ($\lesssim$0.3 rad), but this can be comparable to the difference between NR waveforms at different extraction radius (see Fig. 13 in Appendix C). We notice that although the errors in those modes are not as small as those of the modes (2,1) and (3,3), they are still acceptable considering the relatively

[7]The subscript "c" means "constrained" while "f" stands for "free".

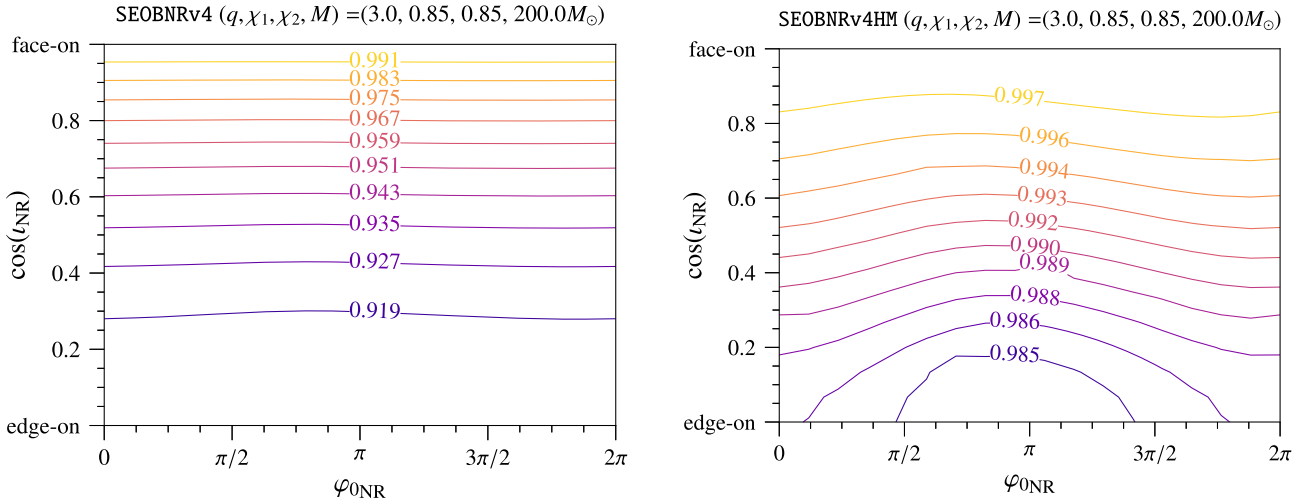

FIG. 6. Faithfulness $\mathcal{F}(\cos(\iota_{\rm NR}),\varphi_{0\rm NR},\kappa_{\rm NR}=0)$ for the configuration $(q=3,M=200\,M_\odot,\chi_1=0.85,\chi_2=0.85)$: NR $(\ell\leq 5,m\neq 0)$ vs SEOBNRv4 (left panel), NR $(\ell\leq 5,m\neq 0)$ vs SEOBNRv4HM (right panel). We plot the faithfulness for a fixed $\kappa_{\rm NR}$ because we have noted that $\mathcal{F}(\iota_{\rm NR},\varphi_{0\rm NR},\kappa_{\rm NR})$ is mildly dependent on this variable.

small amplitude of the modes (4,4) and (5,5) with respect to the (2,1) and (3,3).

In summary, given a binary configuration (m_1, m_2,χ_1,χ_2), the merger-ringdown model that we have developed is uniquely determined by the following parameters $(m_1,m_2,\chi_1,\chi_2,t^{\ell m}_{\rm match},\phi^{\ell m}_{\rm match},\sigma^{\rm I}_{\ell m},\sigma^{\rm R}_{\ell m})$, the latter being a function of the remnant-BH's mass and spin determined by the NR fits. It is possible to use this merger-ringdown model as a stand-alone model (i.e., independently from the inspiral-plunge part), if we also provide equations relating $\phi^{\ell m}_{\rm match}$ [i.e., the phase of the mode (ℓ,m) at $t^{\ell m}_{\rm match}$] with $\phi^{22}_{\rm match}$. Indeed even if a global time and phase shift is possible, the relations between the phases of different modes are fixed. The latter are given as a fit for every point of the parameter space (ν,χ_1,χ_2) in Appendix D. We note that in this stand-alone merger-ringdown model, one can also treat $\sigma^{\rm I}_{\ell m}$ and $\sigma^{\rm R}_{\ell m}$ as free parameters (i.e., we do not compute them from Refs. [69,93]). In this case the merger-ringdown model is a function of $(m_1,m_2,\chi_1,\chi_2,t^{\ell m}_{\rm match},\phi^{\ell m}_{\rm match},\sigma^{\rm I}_{\ell m},\sigma^{\rm R}_{\ell m},M_{\rm final})$ where $M_{\rm final}$ is the remnant-BH's, which is used only to rescale $\sigma^{\rm I}_{\ell m}$ and $\sigma^{\rm R}_{\ell m}$.

V. PERFORMANCE OF THE MULTIPOLAR EFFECTIVE-ONE-BODY WAVEFORM MODEL

We study the accuracy of the multipolar waveform model SEOBNRv4HM by computing its faithfulness against waveforms in the NR catalog at our disposal. In Secs. V A and V B, we perform a detailed comparison against three NR simulations, notably a moderate–mass-ratio configuration, SXS:BBH:0293 $(q=3,\chi_1=0.85,\chi_2=0.85)$, and two high–mass-ratio configurations, SXS:BBH:0065 $(q=8,\chi_1=0.5,\chi_2=0)$ and ET:AEI:0004 $(q=8,\chi_1=0.85,\chi_2=0.85)$. We also compare the results above with those obtained when the (2,2)–waveform-model SEOBNRv4 is employed. Finally, in Sec. V C we summarize the agreement of the SEOBRNv4HM model against the entire NR catalog composed of 157 simulations.

A. Moderate mass ratio: SXS:BBH:0293

In the left panel of Fig. 6 we show a contour plot of the faithfulness $\mathcal{F}(\cos(\iota_{\rm NR}),\varphi_{0\rm NR},\kappa_{\rm NR})|_{\kappa_{\rm NR}=0}$ between the NR waveform SXS:BBH:0293 with modes $(\ell\leq 5,\ m\neq 0)$, and the waveform generated with SEOBNRv4, for a total mass of $M=200\ M_\odot$. In order to reduce the dimensionality of the plot, we fix the value of $\kappa_{\rm NR}$. However, we find that the dependence of the faithfulness on this variable is mild. We can see that the faithfulness depends mainly on the inclination angle $\iota_{\rm NR}$ and degrades when we move from a face-on $\{\mathcal{F}(\cos(\iota_{\rm NR})=0)\sim 99\%\}$ to an edge-on orientation $\{\mathcal{F}(\cos(\iota_{\rm NR})=1)\sim 92\%\}$. This situation is different if we include the higher-order modes in the model [i.e., (3,3), (2,1), (4,4), (5,5)], as can be seen in the right panel of Fig. 6 where we use the SEOBNRv4HM waveform model. In this case the faithfulness degrades much less if we go from a face-on ($\mathcal{F}\sim 99.7\%$) to an edge-on ($\mathcal{F}\sim 98.5\%$) orientation. The small residual degradation is due to the fact that the dominant mode is still better modeled than the higher-order modes and for this reason for a face-on orientation (where the signal is dominated by the dominant mode) the faithfulness is larger than for an edge-on orientation where the higher-order modes contribute the most. Another contribution to the residual degradation in an edge-on orientation stems from the fact that in the SEOBNRv4HM model we still miss some subdominant higher-order modes, which instead we have included in the NR waveform.

As done in Sec. III we summarize the results of the faithfulness calculation in Fig. 7, where we show the

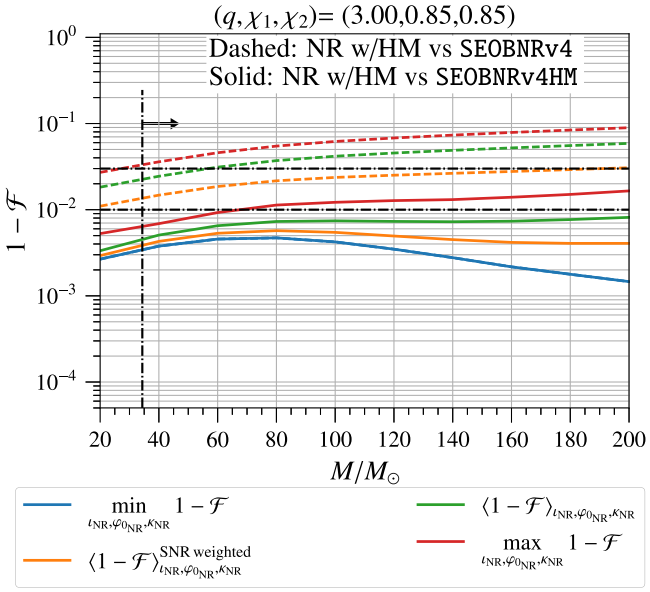

FIG. 7. Unfaithfulness $(1-\mathcal{F})$ for the configuration $(q=3,\chi_1=\chi_2=0.85)$ in the mass range $20\,M_\odot \le M \le 200\,M_\odot$. Dashed (plain) curves refer to results for SEOBNRv4 (SEOBNRv4HM). The minima of the unfaithfulness for the two models (blue curves), lie on top of each other because they are reached for a face-on orientation, where the higher modes contribution is zero. The unfaithfulness averaged over the three angles $\iota_{NR},\varphi_{0NR},\kappa_{NR}$ are obtained assuming an isotropic distribution for the source orientation, homogeneous distribution in GW polarization and isotropic distribution in sky position (green curves and orange curves for the average weighted with the SNR). The minimum of the unfaithfulness (red curves) in practice correspond to an edge-on orientation, minimized over the other two angles. The vertical dotted-dashed black line is the smallest mass at which the (2,1) mode is entirely in the Advanced LIGO band. The (ℓ,m') mode is entirely in the Advanced LIGO band starting from a mass m' times the mass associated with the (2,1) mode. The horizontal dotted-dashed black lines represent the values of 1% and 3% unfaithfulness.

minimum and maximum of the unfaithfulness over the NR orientations, GW polarization and sky position, respectively indicated as $\min_{\iota_{NR},\varphi_{0NR},\kappa_{NR}}(1-\mathcal{F})$ (blue) and $\max_{\iota_{NR},\varphi_{0NR},\kappa_{NR}}(1-\mathcal{F})$ (red); the average of the unfaithfulness over these three angles $\langle 1-\mathcal{F}\rangle_{\iota_{NR},\varphi_{0NR},\kappa_{NR}}$ (green), and the average of the unfaithfulness weighted with the cube of the SNR: $\langle 1-\mathcal{F}\rangle^{\text{SNRweighted}}_{\iota_{NR},\varphi_{0NR},\kappa_{NR}}$ (orange). All the averages are computed assuming an isotropic distribution for the source orientation, homogeneous distribution in GW polarization and isotropic distribution in sky position. All these quantities are shown as a function of the total mass of the system. In the plots the plain curves are the results of the unfaithfulness between the NR and SEOBNRv4HM waveforms, while dashed curves are the results of the unfaithfulness between NR and SEOBNRv4 waveforms. In this case, the maximum and the averaged values of the unfaithfulness for the SEOBNRv4 model are one order of magnitude larger than the ones with the SEOBNRv4HM model. The minimum of the unfaithfulness is the same for both models (blue curves lying on top of each other) because it is reached for a face-on orientation, where the contribution of the higher-order modes used for SEOBNRv4HM is zero. Indeed the -2 spin-weighted spherical harmonics associated to these higher-order modes go to zero for face-on orientations. We note also that in SEOBNRv4, as expected, the disagreement grows strongly with the total mass of the system, because higher-order modes are more important toward merger and ringdown.

B. High mass ratios: SXS:BBH:0065 and ET:AEI:0004

More striking conclusions about the improvement of the waveform model due to the inclusion of higher-order modes can be drawn looking at the comparison with the two NR simulations SXS:BBH:0065 and ET:AEI:0004, for which higher-order modes are expected to be more important, because of the higher mass ratio. For the first configuration $(q=8,M=200\,M_\odot,\chi_1=0.5,\chi_2=0)$ we see in Fig. 8 that the faithfulness between the NR $(\ell \le 5, m \ne 0)$ and the SEOBNRv4 waveforms (left panel) degrades much faster than before as a function of the inclination angle ι_{NR}, reaching $\mathcal{F} \lesssim 90\%$ already for values of $\cos(\iota_{NR}) \sim 0.7$ ($\iota_{NR} \sim 45°$), being very large for the edge-on inclination $\mathcal{F} \sim 80\%$. Similarly to what happens for the example discussed in Sec. V A, the situation is much better if we include in the model the higher modes, as can be seen in Fig. 8 (right panel). Now, the degradation as a function of ι_{NR} is much weaker and for edge-on orientations the faithfulness reaches values close to $\mathcal{F} \sim 98\%$. Similar conclusions can be drawn by looking at Fig. 9, which refers to the simulation ET:AEI:0004 $(q=8,M=200\,M_\odot,\chi_1=0.85,\chi_2=0.85)$. The only relevant difference with respect to the aforementioned case is that in this case the faithfulness of the SEOBNRv4HM waveform is a little bit smaller and it goes down to $\mathcal{F} \sim 97.7\%$ in the edge-on orientations. At a fixed binary orientation, the faithfulness of the (2,2)–waveform-model SEOBNRv4 against the NR waveform for the configuration $(q=8,M=200\,M_\odot,\chi_1=0.85=\chi_2=0.85)$ is always larger than that for the configuration $(q=8,M=200\,M_\odot,\chi_1=0.5,\chi_2=0)$. This can be explained considering that, as discussed in Sec. II, for a fixed mass ratio the (2,1) mode is increasingly suppressed when the spin of the heavier BH grows, while the other higher-order modes are mostly constant as a function of the spins. Since in the first case χ_1, that is the spin of the heavier BH, is larger than in the second case, the (2,1) mode is more suppressed in the first case than in the second one. For this reason the faithfulness with the SEOBNRv4 model, including only the dominant mode, is higher for the first configuration.

As for the previous configuration, in Fig. 10, we show the summary of the faithfulness results as maximum,

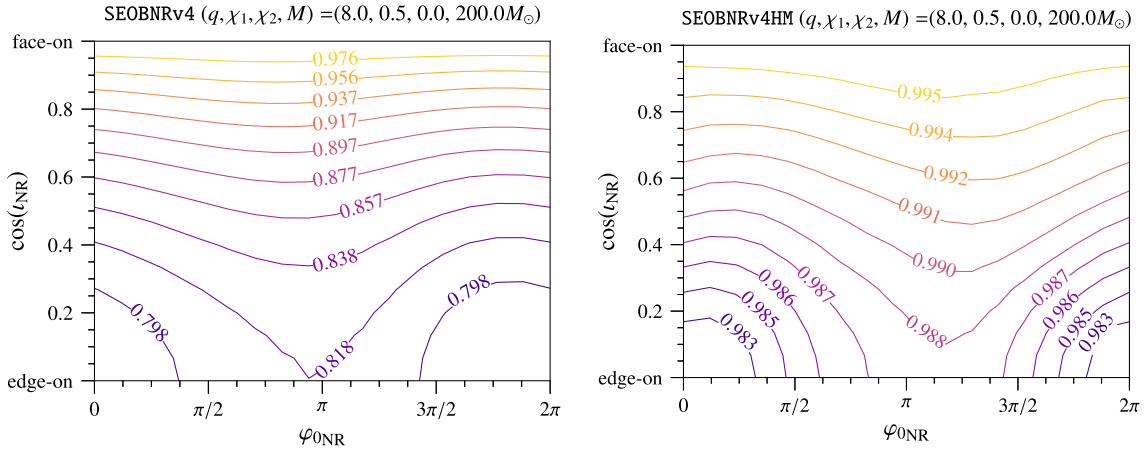

FIG. 8. Faithfulness $\mathcal{F}(\cos(\iota_{\rm NR}),\varphi_{0\rm NR},\kappa_{\rm NR}=0)$ for the configuration $(q=8,M=200\ M_\odot,\chi_1=0.5,\chi_2=0)$: NR $(\ell\leq 5,m\neq 0)$ vs SEOBNRv4 (left panel), NR $(\ell\leq 5,m\neq 0)$ vs SEOBNRv4HM (right panel).

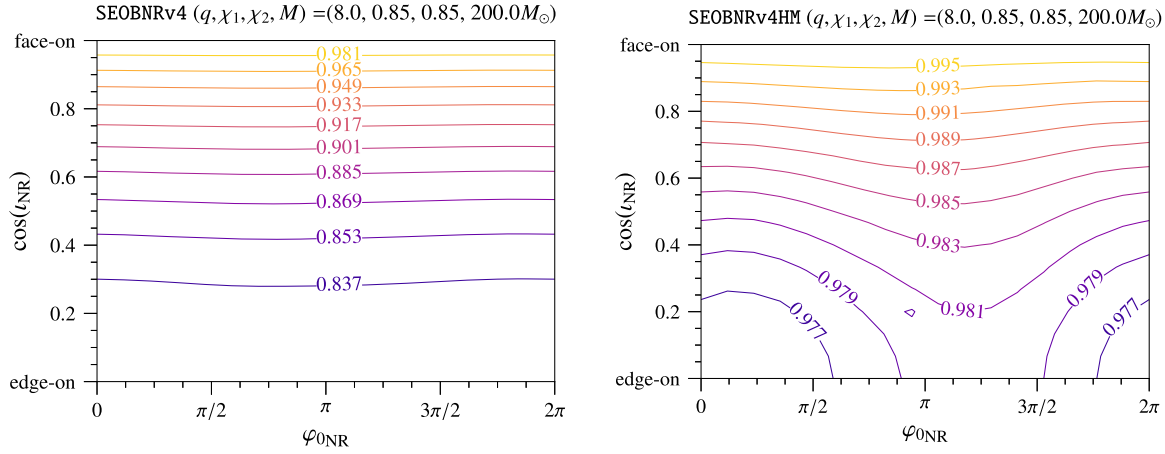

FIG. 9. Faithfulness $\mathcal{F}(\cos(\iota_{\rm NR}),\varphi_{0\rm NR},\kappa_{\rm NR}=0)$ for the configuration $(q=8,M=200\ M_\odot,\chi_1=0.85,\chi_2=0.85)$: NR $(\ell\leq 5,m\neq 0)$ vs SEOBNRv4 (left panel), NR $(\ell\leq 5,m\neq 0)$ vs SEOBNRv4HM (right panel).

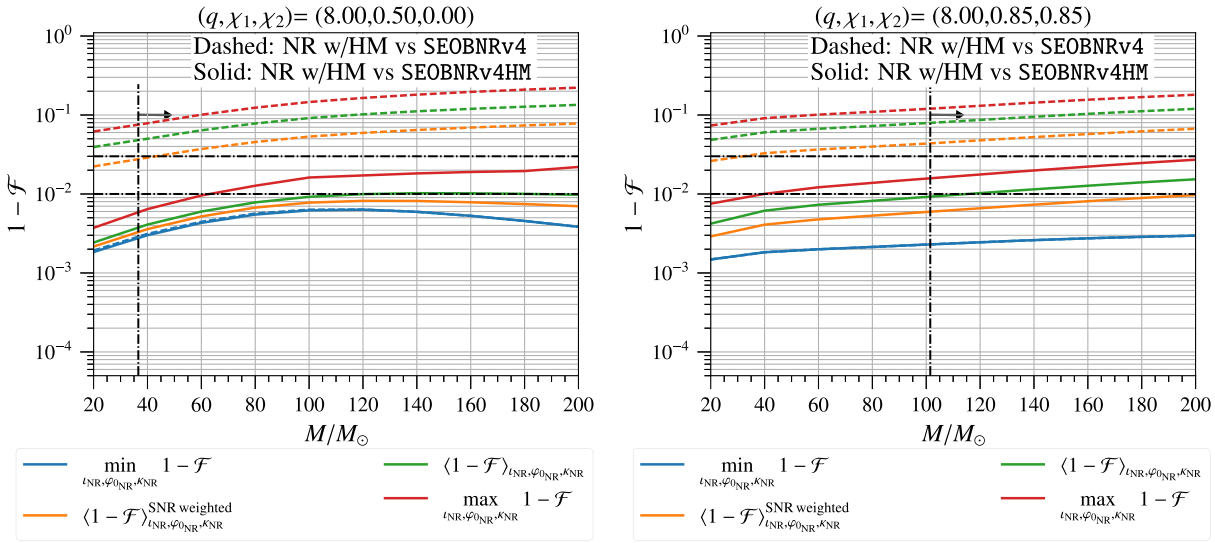

FIG. 10. Unfaithfulness $(1-\mathcal{F})$ in the mass range $20\ M_\odot\leq M\leq 200\ M_\odot$ for the configuration $(q=8,\chi_1=0.5,\chi_2=0)$ (left panel) and $(q=8,\chi_1=0.85,\chi_2=0.85)$ (right panel). Plotted data as in Fig. 7.

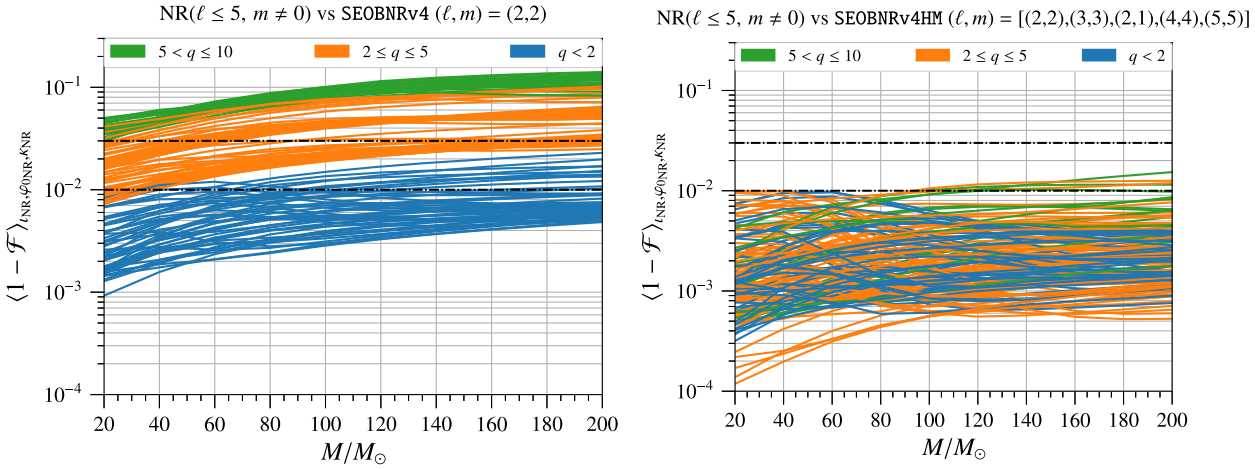

FIG. 11. Unfaithfulness $(1-\mathcal{F})$ averaged over the three angles $(\iota_{NR}, \varphi_{0NR}, \kappa_{NR})$ as a function of the total mass, in the range $20\ M_\odot \leq M \leq 200\ M_\odot$. Left panel NR $(\ell \leq 5, m \neq 0)$ vs SEOBNRv4, right panel NR $(\ell \leq 5, m \neq 0)$ vs SEOBNRv4HM. The horizontal dotted-dashed black lines represent the values of 1% and 3% unfaithfulness.

minimum and averages of the unfaithfulness, respectively for SXS:BBH:0065 (left panel) and ET:AEI:0004 (right panel). For these binary configurations, even if the maxima of the unfaithfulness have larger values with respect to the case discussed in the previous section (∼2% for SXS:BBH:0065 and ∼2.7% for ET:AEI:0004 at a total mass of $M = 200\ M_\odot$), we still have acceptable values of the unfaithfulness averaged over the orientations, sky position and polarizations: respectively ∼1% and ∼1.6% for a total mass of $M = 200\ M_\odot$. This is a big improvement with respect to the SEOBNRv4 model, which gives averaged values of the unfaithfulness larger than 10% for both configurations and the same total mass. For the configuration with $q = 8, \chi_1 = 0.85 = \chi_2 = 0.85$, the unfaithfulness against the NR simulation was also computed for the multipolar waveform model developed in Ref. [47], and found to be around ∼5% for $\iota_s = \pi/2$, when averaging over the angles κ_s and φ_{0s} for a total mass $M = 100\ M_\odot$. In our model the maximum of the unfaithfulness (i.e., $\max_{\iota_s,\varphi_{0s},\kappa_s}(1-\mathcal{F})$) over the angles ι_s, φ_{0s} and κ_s is around 1.5% at $M = 100\ M_\odot$. The reason for the better accuracy of SEOBNRv4HM model with respect to the waveform model in Ref. [47] for this "extreme" binary configuration might be due to the fact that the simple scaling argument used there to build the higher-order modes is not very accurate for high-mass ratio and high-spin binary systems. We leave to the future a direct, comprehensive comparison between the two waveform models.

As discussed in Sec. III, an important quantity to assess the improvement that SEOBNRv4HM could yield for detecting BBHs is the average unfaithfulness weighted with the cube of the SNR. For this quantity our model yields values of ∼0.7% for SXS:BBH:0065 and ∼1% for ET:AEI:0004 at a total mass of $M = 200\ M_\odot$ compared to values around ∼7% returned by the SEOBNRv4 model.

C. Comparison with entire numerical-relativity catalog

Having studied in detail some particular configurations, we can now examine how the model works over the entire NR waveform catalog at our disposal. In Fig. 11 we plot the angle-averaged unfaithfulness as a function of the total mass of the system, computed between the NR waveforms with modes $(\ell \leq 5, m \neq 0)$ and the SEOBNRv4 model (left panel), SEOBNRv4HM model (right panel). Comparing the two panels, we can see that SEOBNRv4HM yields unfaithfulnesses one order of magnitude smaller than those of the SEOBNRv4 model. In the plots different colors correspond to different ranges of mass ratios, and from the left panel it is visible that in the case of the SEOBNRv4 model, there is a clear hierarchy for which configurations with higher mass ratios have also larger unfaithfulness. This effect is removed in the SEOBNRv4HM model, as visible in the right panel of the same figure. In general for all of NR simulations the averaged unfaithfulness against SEOBNRv4HM is always smaller than 1% in the mass range $20\ M_\odot \leq M \leq 200\ M_\odot$ with the exception of few simulations for which the unfaithfulness reaches values ≤1.5% for a total mass of $M = 200\ M_\odot$: SXS:BBH:0202 $(q=7, \chi_1=0.6, \chi_2=0)$, ET:AEI:0004 $(q=8, \chi_1=0.85, \chi_2=0.85)$, ET:AEI:0001 $(q=5, \chi_1=0.8, \chi_2=0)$ and SXS:BBH:0061 $(q=5, \chi_1=0.5, \chi_2=0)$. These are the configurations in the NR catalog having the most extreme values of mass ratio and spins. The results of this analysis does not change considerably if we include in the NR waveforms only the modes used in the SEOBNRv4HM model, because, when looking at averaged unfaithfulness, the error is dominated by the imperfect modeling of the (2,1), (3,3), (4,4), (5,5) modes, and not by neglecting other subdominant higher modes, as discussed in Sec. III.

The comparison between the unfaithfulness averaged over the three angles $(\iota_{NR}, \varphi_{0NR}, \kappa_{NR})$ and weighted by the cube of the SNR of two waveform models against NR

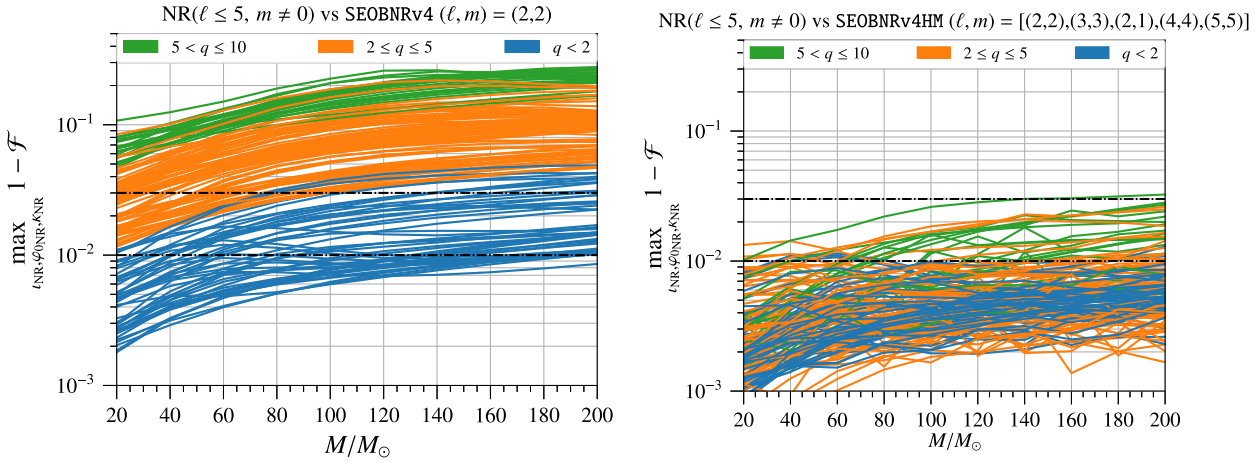

FIG. 12. Maximum of unfaithfulness $(1 - \mathcal{F})$ over the three angles $(\iota_{NR}, \varphi_{0NR}, \kappa_{NR})$ as a function of the total mass, in the range $20\ M_\odot \leq M \leq 200\ M_\odot$. Left panel NR $(\ell \leq 5, m \neq 0)$ vs SEOBNRv4, right panel NR $(\ell \leq 5, m \neq 0)$ vs SEOBNRv4HM. The horizontal dotted-dashed black lines represent the values of 1% and 3% unfaithfulness. The jaggedness of the curves in the plot (right panel) is caused by the numerical noise present in the NR higher-order modes, which are not very well resolved. We find that this feature is not present when these noisy modes are removed from the calculation of the faithfulness.

waveforms displays similar features, with the only difference of having overall smaller values of the unfaithfulness (always ≤1% for the SEOBNRv4HM model). This happens because weighting with the SNR favors orientations closer to face-on for which the best modeled (2,2) mode is dominant.

Finally, in the right panel of Fig. 12 we show the maximum of the unfaithfulness over the three angles $(\iota_{NR}, \varphi_{0NR}, \kappa_{NR})$ between the SEOBNRv4HM model and the NR waveforms with the modes $(\ell \leq 5, m \neq 0)$. In the left panel of the same figure we show the same comparison but this time using the SEOBNRv4 model. Here we see that the SEOBNRv4HM waveforms have unfaithfulness smaller than 3% in the mass range considered for all the NR simulations with the exception of one case, namely SXS:BBH:0621 $(q = 7, \chi_1 = -0.8, \chi_2 = 0)$ for which the unfaithfulness at $M = 200\ M_\odot$ is $(1 - \mathcal{F}) \sim 3.1\%$.

In general, over the NR simulations of our catalog, the maximum of the unfaithfulness is always smaller than 1% in the total mass range $20\ M_\odot \leq M \leq 200\ M_\odot$ for nonspinning configurations up to mass ratio $q = 8$. Nonspinning cases with $q \geq 8$ and configurations with high spins and mass ratios $q \geq 5$ have maximum unfaithfulness in the range $1\% \leq (1 - \mathcal{F}) \leq 3\%$. For the former the unfaithfulness decreases to values smaller than 1% when the comparison is done including only the modes (2,2), (2,1), (3,3), (4,4), (5,5) in the NR waveforms [i.e., excluding smaller higher-order modes like (3,2), (4,3)]. This is not true for high-spin, high–mass-ratio configurations where the unfaithfulness due to a nonperfect modeling dominates over that due to neglecting smaller higher-order modes. It is important to stress that, as discussed in Sec. III, the maximum unfaithfulness due to the numerical error in the NR waveforms of our catalog is in the range $[0.1\%, 1\%]$. This means that when comparing the NR waveforms with the SEOBNRv4HM model a fraction of the maximum unfaithfulness as large as 1% could be due to numerical error. Given that maximum unfaithfulness are reached for edge-on configurations where the higher-order modes are more relevant, NR waveforms with better resolved higher-order modes would be needed in order to attempt to build a model with maximum unfaithfulness smaller than 1%.

VI. CONCLUSIONS

We have worked within the spinning EOB framework and have built a multipolar waveform model for BBHs with nonprecessing spins that includes the higher-order modes $(\ell, m) = (2,1), (3,3), (4,4), (5,5)$, besides the dominant (2,2) mode. In order to improve the agreement with the NR results we included recently computed PN corrections [48,49,97] in the resummed GW modes, and also used nonperturbative informations from NR waveforms in the NQCs corrections of the higher-order modes, and in the calibration parameters $c_{\ell m}$'s [the latter only for the modes (2,1), (5,5)]. We also extended to higher-order modes the phenomenological ansatz for the merger-ringdown signal that was originally proposed in Refs. [27,63,64,66] for the dominant (2,2) mode.

We have found that the unfaithfulness averaged over orientations, polarizations and sky positions between the SEOBNR4HM model and NR waveforms of the catalog at our disposal, is always smaller than 1% with the exception of four configurations for which the unfaithfulness is smaller than 1.5%. Moreover, the unfaithfulness are one order of magnitude smaller than those obtained with the SEOBNRv4 model [27], which only contains the (2,2) mode. The maximum unfaithfulness over orientations, polarizations and sky positions between SEOBNR4HM and NR waveforms is always smaller than 3% with the exception of one configuration for which the faithfulness is smaller than 3.1%. Also for the maximum unfaithfulness the results are

one order of magnitude smaller than those obtained with the SEOBNRv4 model [27]. We have also found that, in the nonspinning limit, the SEOBNRv4HM model returns values of the unfaithfulness smaller than its (nonspinning) predecessor waveform model, that is EOBNRv2HM [45] (see Appendix G).

Other studies are needed to fully assess the accuracy of SEOBNRv4HM for GW astronomy. In particular it will be important to understand if unfaithfulnesses below 1% can affect the recovery of binary parameters, and if so which parameters will be mainly biased, for which SNR and in which region of the parameter space. In particular, we expect that the multipolar SEOBNRv4HM model will be more precise than the SEOBNRv4 model for recovering the binary's inclination angle and the distance from the source. Indeed, those parameters are degenerate with each other when only the (2,2) mode is present, and the inclusion of higher-order modes can help in disentangle them (e.g., see Ref. [98]). We postpone this kind of studies to the future because for computational reasons, we would need to develop a reduced-order-model (ROM) [26] version of the SEOBNRv4HM model. Another important test for the future would be the comparison between SEOBNRv4HM model and other multipolar, inspiral-merger-ringdown in the literature, such as the IMRPhenom models proposed in Refs. [46,47]. It will be relevant to compare those models especially outside the range of binary configurations where the NR waveforms are available, in order to identify if there are regions where the two models predict significantly different waveforms.

We also expect that the multipolar spinning, nonprecessing waveform model developed here will be a more accurate model to carry out parameterized tests of general relativity [30] when BBHs with high mass-ratio, high total mass and in a non face-on orientation will be detected. Furthermore, the SEOBNRv4HM model can be employed to search for more than one gravitational quasi-normal mode in the ringdown portion of the signal, coherently with multiple detections [68–71]. In fact, those studies can also be performed with our multipolar, stand-alone merger-ringdown model.

The SEOBNRv4HM waveform model employs the same conservative and dissipative dynamics of the SEOBNRv4 model, which was calibrated to NR simulations by requiring very good agreement with the NR (2,2) GW mode. Further improvements of the SEOBNRv4 waveform model could be achieved in the future by recalibrating the two-body dynamics. Such calibration would require the production of a new set of NR waveforms (with more accurate higher-order modes) in the region of high mass-ratios, say $q \geq 4$, and high spins, say $\chi_{1,2} \geq 0.6$ where few NR simulations are currently available and where the disagreement between current analytical inspiral-merger-ringdown waveforms is the worst (e.g., see Figs. 5 and 6 in Ref. [27]). Those NR waveforms would need to be sufficiently long to make the calibration procedure sufficiently robust (see Sec. VI, and Figs. 7 and 8 in Ref. [27]).

In the near future our priority is to include the next largest modes in the SEOBNRHM model, notably the (3,2), (4,3) modes. The work would need to take into account the mixing between spherical-harmonic and spheroidal harmonics during the merger-ringdown stage, as observed in Refs. [83,84], and investigated more recently in Refs. [65,85]. Insights might need to be gained also from merger-ringdown waveforms in the test-particle limit [99–101]. However, to develop a more accurate multipolar model, one would also need to reduce the numerical error in NR waveforms around merger and during ringdown, in particular for the modes (4,4) and (5,5). Another important and timely application of this work, is its extension to the spinning, precessing case, thus improving, the current SEOBNRv3 model [31,32,102], which only contains the (2,2) and (2,1) modes.

ACKNOWLEDGMENTS

It is a pleasure to thank Juan Calderon Bustillo, Ian Harry, Sylvain Marsat, Harald Pfeiffer, and Noah Sennett for helpful discussions. Computational work for this manuscript was carried out on the computer clusters Vulcan and Minerva at the Max Planck Institute for Gravitational Physics in Potsdam.

APPENDIX A: EXPLICIT EXPRESSIONS OF HIGHER-ORDER *FACTORIZED* MODES

Here we list expressions needed to build the $h_{\ell m}$'s of the SEOBNRv4HM model.

The functions $n^{(\epsilon)}_{\ell m}$ and $c_{\ell+\epsilon}(\nu)$ used in Eq. (4.7) are defined as (see Ref. [103]):

$$n^{(0)}_{\ell m} = (im)^{\ell} \frac{8\pi}{(2\ell+1)!!} \sqrt{\frac{(\ell+1)(\ell+2)}{\ell(\ell-1)}}, \tag{A1}$$

$$n^{(0)}_{\ell m} = -(im)^{\ell} \frac{16\pi i}{(2\ell+1)!!} \sqrt{\frac{(2\ell+1)(\ell+2)(\ell^2-m^2)}{(2\ell-1)(\ell+1)\ell(\ell-1)}}, \tag{A2}$$

and

$$c_{\ell+\epsilon}(\nu) = \left(\frac{1}{2} - \frac{1}{2}\sqrt{1-4\nu}\right)^{\ell+\epsilon-1} + (-1)^{\ell+\epsilon}\left(\frac{1}{2} + \frac{1}{2}\sqrt{1-4\nu}\right)^{\ell+\epsilon-1}. \tag{A3}$$

We define also the function

$$\mathrm{eulerlog}(m, v_\Omega) \equiv \gamma + \log(2 m v_\Omega), \tag{A4}$$

which is used in the expression of the factorized modes. Here γ is the Euler constant.

The quantity $f_{\ell m}$ in Eq. (4.5) is:

$$f_{\ell m} = \begin{cases} \rho^{\ell}_{\ell m}, & \ell \text{ is even}, \\ (\rho^{\mathrm{NS}}_{\ell m})^{\ell} + f^{\mathrm{S}}_{\ell m}, & \ell \text{ is odd}. \end{cases} \tag{A5}$$

The functions $\rho_{\ell m}$, $\rho^{\rm NS}_{\ell m}$, $f^{\rm S}_{\ell m}$ are defined below; the superscript "NS" stands for nonspinning, and the superscript "S" indicates spinning. Below, we also list the phase terms $\delta_{\ell m}$.

The quantities $f_{\ell m}$ and $\delta_{\ell m}$ for the `SEOBNRv4HM` model are mostly taken from the `SEOBNRv4` model in Ref. [27] with the additions of several new terms:

(i) 3PN nonspinning terms in $\rho^{\rm NS}_{33}$ from Ref. [97];
(ii) 5PN test-mass, nonspinning terms in $\rho^{\rm NS}_{33}$ from Ref. [49];
(iii) 5PN test-mass, nonspinning terms in $\rho^{\rm NS}_{21}$ from Ref. [49];
(iv) 2PN and 2.5PN spinning terms in ρ_{44} from Ref. [48];
(v) 3PN, 4PN and 5PN test-mass, nonspinning terms in $\rho^{\rm NS}_{55}$ from Ref. [49];
(vi) 2PN, 2.5PN and 3PN spinning terms in $f^{\rm S}_{33}$ from Ref. [48];
(vii) 2PN, 2.5PN and 3PN spinning terms in $f^{\rm S}_{21}$ from Ref. [48];
(viii) 1.5PN and 2PN spinning terms in $f^{\rm S}_{55}$ from Ref. [48];
(ix) 3PN and 4.5PN test-mass, nonspinning terms in δ_{55} from Ref. [49].

Furthermore, we find that resummations of the $f_{\ell m}$ function for the (3,3), (2,1), (4,4), (5,5) modes of the kind proposed in Refs. [91,92] [see Eqs. (47) and (48) in the latter] do not always improve the agreement with the NR waveforms of our catalog. For this reason we decide not to implement those resummations when building the `SEOBNRv4HM` model. It is worthwhile to mention that whereas in our model the resummed expressions are computed as a function of $v_\Omega = (M\Omega)^{1/3}$, in Refs. [91,92] they are expressed as a function of v_ϕ defined in Eq. (69) of Ref. [104]. While the two variables are very similar at low frequency, they can differ toward merger where the aforementioned resummation may be more effective.

$$\rho^{\rm NS}_{33} = 1 + \left(-\frac{7}{6} + \frac{2\nu}{3}\right)v_\Omega^2 + \left(-\frac{6719}{3960} - \frac{1861\nu}{990} + \frac{149\nu^2}{330}\right)v_\Omega^4 + \left[\frac{3203101567}{227026800} + \left(-\frac{129509}{25740} + \frac{41\pi^2}{192}\right)\nu - \frac{274621\nu^2}{154440} + \frac{12011\nu^3}{46332} - \frac{26}{7}\,\text{eulerlog}(3, v_\Omega)\right]v_\Omega^6 + \left(-\frac{57566572157}{8562153600} + \frac{13}{3}\,\text{eulerlog}(3, v_\Omega)\right)v_\Omega^8 + \left(-\frac{903823148417327}{30566888352000} + \frac{87347\,\text{eulerlog}(3, v_\Omega)}{13860}\right)v_\Omega^{10}, \tag{A6}$$

$$\rho^{\rm NS}_{21} = 1 + \left(-\frac{59}{56} + \frac{23\nu}{84}\right)v_\Omega^2 + \left(-\frac{47009}{56448} - \frac{10993\nu}{14112} + \frac{617\nu^2}{4704}\right)v_\Omega^4 + \left(\frac{7613184941}{2607897600} - \frac{107}{105}\,\text{eulerlog}(1, v_\Omega)\right)v_\Omega^6 + \left(-\frac{1168617463883}{911303737344} + \frac{6313\,\text{eulerlog}(1, v_\Omega)}{5880}\right)v_\Omega^8 + \frac{(-63735873771463 + 14061362165760\,\text{eulerlog}(1, v_\Omega))v_\Omega^{10}}{16569158860800}, \tag{A7}$$

$$\begin{aligned}\rho_{44} = 1 &+ \left(\frac{1614 - 5870\nu + 2625\nu^2}{1320(-1+3\nu)}\right)v_\Omega^2 + \left[\left(\frac{2}{3(-1+3\nu)} - \frac{41\nu}{15(-1+3\nu)} + \frac{14\nu^2}{5(-1+3\nu)}\right)\chi_S + \delta m\left(\frac{2}{3(-1+3\nu)} - \frac{13\nu}{5(-1+3\nu)}\right)\chi_A\right]v_\Omega^3 \\ &+ \left[-\frac{14210377}{8808800(1-3\nu)^2} + \frac{32485357\nu}{4404400(1-3\nu)^2} - \frac{1401149\nu^2}{1415700(1-3\nu)^2} - \frac{801565\nu^3}{37752(1-3\nu)^2} + \frac{3976393\nu^4}{1006720(1-3\nu)^2} + \frac{\chi_A^2}{2} - 2\nu\chi_A^2 + \delta m\chi_A\chi_S + \frac{\chi_S^2}{2}\right]v_\Omega^4 \\ &+ \left[\left(-\frac{69}{55(1-3\nu)^2} + \frac{16571\nu}{1650(1-3\nu)^2} - \frac{2673\nu^2}{100(1-3\nu)^2} + \frac{8539\nu^3}{440(1-3\nu)^2} + \frac{591\nu^4}{44(1-3\nu)^2}\right)\chi_S + \delta m\left(-\frac{69}{55(1-3\nu)^2} + \frac{10679\nu}{1650(1-3\nu)^2} - \frac{1933\nu^2}{220(1-3\nu)^2} + \frac{597\nu^3}{440(1-3\nu)^2}\right)\chi_A\right]v_\Omega^5 \\ &+ \left(\frac{16600939332793}{1098809712000} - \frac{12568\,\text{eulerlog}(4, v_\Omega)}{3465}\right)v_\Omega^6 + \left(-\frac{172066910136202271}{19426955708160000} + \frac{845198\,\text{eulerlog}(4, v_\Omega)}{190575}\right)v_\Omega^8 \\ &+ \left(-\frac{17154485653213713419357}{568432724020761600000} + \frac{22324502267\,\text{eulerlog}(4, v_\Omega)}{3815311500}\right)v_\Omega^{10},\end{aligned} \tag{A8}$$

$$\rho_{55}^{\rm NS} = 1 + \left(\frac{487}{390(-1+2\nu)} - \frac{649\nu}{195(-1+2\nu)} + \frac{256\nu^2}{195(-1+2\nu)}\right)v_\Omega^2 - \frac{3353747 v_\Omega^4}{2129400} + \left(\frac{190606537999247}{11957879934000} - \frac{1546}{429}\text{eulerlog}(5, v_\Omega)\right)v_\Omega^6 + \left(-\frac{12136419599492914 37}{118143853747920000} + \frac{376451\text{eulerlog}(5, v_\Omega)}{83655}\right)v_\Omega^8 + \left(-\frac{150082616449726042201261}{4837990810977324000000} + \frac{2592446431\text{eulerlog}(5, v_\Omega)}{456756300}\right)v_\Omega^{10}, \tag{A9}$$

$$f_{33}^{\rm S} = \left[\left(-2+\frac{19\nu}{2}\right)\frac{\chi_A}{\delta m} + \left(-2+\frac{5\nu}{2}\right)\chi_S\right]v_\Omega^3 + \left[\left(\frac{3}{2}-6\nu\right)\chi_A^2 + (3-12\nu)\frac{\chi_A}{\delta m}\chi_S + \frac{3\chi_S^2}{2}\right]v_\Omega^4 + \left[\left(\frac{2}{3}-\frac{593\nu}{60}+\frac{407\nu^2}{30}\right)\frac{\chi_A}{\delta m} + \left(\frac{2}{3}+\frac{11\nu}{20}+\frac{241\nu^2}{30}\right)\chi_S\right]v_\Omega^5 + \left[\left(-\frac{7}{4}+\frac{11\nu}{2}-12\nu^2\right)\chi_A^2 + \left(-\frac{7}{2}-\nu+44\nu^2\right)\frac{\chi_A}{\delta m}\chi_S + \left(-\frac{7}{4}-\frac{27\nu}{2}+6\nu^2\right)\chi_S^2\right]v_\Omega^6 + \left[\left(-\frac{81}{20}+\frac{7339\nu}{540}\right)\frac{\chi_A}{\delta m} + \left(-\frac{81}{20}+\frac{593\nu}{108}\right)\chi_S\right]i(H_{\rm EOB}\Omega)^2, \tag{A10}$$

$$f_{21}^{\rm S} = \left(-\frac{3}{2}\chi_S - \frac{3\chi_A}{2\delta m}\right)v_\Omega + \left[\left(\frac{61}{12}+\frac{79\nu}{84}\right)\chi_S + \left(\frac{61}{12}+\frac{131\nu}{84}\right)\frac{\chi_A}{\delta m}\right]v_\Omega^3 + \left[(-3-2\nu)\chi_A^2 + \left(-3+\frac{\nu}{2}\right)\chi_S^2 + \left(-6+\frac{21\nu}{2}\right)\chi_S\frac{\chi_A}{\delta m}\right]v_\Omega^4 + \left\{\left(\frac{3}{4\delta m}-\frac{3\nu}{\delta m}\right)\chi_A^3 + \left[-\frac{81}{16}+\frac{1709\nu}{1008}+\frac{613\nu^2}{1008} + \left(\frac{9}{4}-3\nu\right)\chi_A^2\right]\chi_S + \frac{3\chi_S^3}{4} + \left[-\frac{81}{16}-\frac{703\nu^2}{112}+\frac{8797\nu}{1008} + \left(\frac{9}{4}-6\nu\right)\chi_S^2\right]\frac{\chi_A}{\delta m}\right\}v_\Omega^5 + \left[\left(\frac{4163}{252}-\frac{9287\nu}{1008}-\frac{85\nu^2}{112}\right)\chi_A^2 + \left(\frac{4163}{252}-\frac{2633\nu}{1008}+\frac{461\nu^2}{1008}\right)\chi_S^2 + \left(\frac{4163}{126}-\frac{1636\nu}{21}+\frac{1088\nu^2}{63}\right)\chi_S\frac{\chi_A}{\delta m}\right]v_\Omega^6 + \mathbf{c_{21}}v_\Omega^7, \tag{A11}$$

$$f_{55}^{\rm S} = \left[\left(-\frac{70\nu}{3(-1+2\nu)} + \frac{110\nu^2}{3(-1+2\nu)} + \frac{10}{3(-1+2\nu)}\right)\frac{\chi_A}{\delta m} + \left(\frac{10}{3(-1+2\nu)} - \frac{10\nu}{-1+2\nu} + \frac{10\nu^2}{-1+2\nu}\right)\chi_S\right]v_\Omega^3 + \left[\frac{5}{2}\delta m^2\chi_A^2 + 5\delta m\chi_A\chi_S + \frac{5\chi_S^2}{2}\right]v_\Omega^4 + \mathbf{c_{55}}v_\Omega^5. \tag{A12}$$

$$\delta_{33} = \frac{13}{10}(H_{\rm EOB}\Omega) + \frac{39\pi}{7}(H_{\rm EOB}\Omega)^2 + \left(-\frac{227827}{3000}+\frac{78\pi^2}{7}\right)(H_{\rm EOB}\Omega)^3 - \frac{80897\nu}{2430}v_\Omega^5, \tag{A13}$$

$$\delta_{21} = \frac{2}{3}(\Omega H_{\rm EOB}) + \frac{107}{105}\pi(\Omega H_{\rm EOB})^2 + \left(-\frac{272}{81}+\frac{214\pi^2}{315}\right)\Omega^3 H_{\rm EOB}^3 - \frac{493}{42}\nu v_\Omega^5, \tag{A14}$$

$$\delta_{44} = \frac{(112+219\nu)}{120(1-3\nu)}(\Omega H_{\rm EOB}) + \frac{25136\pi}{3465}(\Omega H_{\rm EOB})^2 + \left(\frac{201088}{10395}\pi^2 - \frac{55144}{375}\right)(\Omega H_{\rm EOB})^3, \tag{A15}$$

$$\delta_{55} = \frac{(96875+857528\nu)}{131250(1-2\nu)}(\Omega H_{\rm EOB}) + \frac{3865\pi}{429}(\Omega H_{\rm EOB})^2 + \frac{-7686949127+954500400\pi^2}{31783752}(\Omega H_{\rm EOB})^3. \tag{A16}$$

We notice that f_{33}^S is a complex quantity because it contains an imaginary term recently computed in PN theory [48]

$$i\delta_{33}^{\rm S} \equiv \left[\left(-\frac{81}{20}+\frac{7339\nu}{540}\right)\frac{\chi_A}{\delta m} + \left(-\frac{81}{20}+\frac{593\nu}{108}\right)\chi_S\right]i(H_{\rm EOB}\Omega)^2, \tag{A17}$$

where with the superscript "S" we indicate the spin dependence. The term proportional to $\chi_A/\delta m$ seems to diverge when $\delta m \to 0$, but this divergence is apparent because, as it happens for all the functions $f^{\rm S}_{\ell m}$, it is removed by the factor δm that appears in the function $c_{\ell+\epsilon}(\nu)$ [see Eq. (A3)] at Newtonian order [see Eq. (4.7)]. If one includes the term $\delta^{\rm S}_{33}$ in the resummation with the complex exponential, one obtains the expression $e^{i(\delta_{33}+\delta^{\rm S}_{33})}$ which is not well-behaved in the limit $\delta m \to 0$. For this reason we do not include this new PN term in the resummation $f_{33}e^{i(\delta_{33}+\delta^{\rm S}_{33})}$, but, instead, we compute the latter quantity excluding this term (i.e., $f_{33}e^{i\delta_{33}}$) and we then add the new complex term to the real amplitude f_{33}. We can do so because $e^{i\delta_{33}} i\delta^{\rm S}_{33} = i\delta^{\rm S}_{33} + \mathcal{O}(\Omega^3)$, where the latter is a PN correction at higher order with respect to the order at which we currently know PN terms.

We remember also that the modes (2,1), (5,5) contain the calibration parameters c_{21} and c_{55} computed imposing the condition in Eq. (4.12).

APPENDIX B: FITS OF NONQUASICIRCULAR INPUT VALUES

We build the fits of the nonquasicircular (NQC) input values using NR waveforms with the highest level of resolution available and the extrapolation order $N = 2$. Depending on the mode, the fits use a different number of NR waveforms, because for some binary configurations the large numerical error prevents us to use some NR modes. For each mode, in order to choose which NR simulations to use for the fits, we first remove all the NR simulations showing clearly unphysical features (e.g., strong oscillations in the post-merger stage that are not consistent among waveforms at different resolution and extrapolation order). For the modes (3,3) and (2,1) all the NR waveforms pass this selection, while for the modes (4,4) and (5,5) we remove respectively 10 and 42 NR simulations. For each NQC input value (i.e., amplitude and its first and second derivative, and frequency and its first derivative) we weight the value extracted by a given NR simulation with the inverse of the NR error. The latter is estimated as $\sqrt{(\delta^{\rm NQC}_{\rm res})^2 + (\delta^{\rm NQC}_{\rm extr})^2}$, where $\delta^{\rm NQC}_{\rm res}$ is the difference between the NQC input values extracted from the NR waveform with the same extrapolation order ($N = 2$) and different resolutions (i.e., the highest and second highest resolution). The quantity $\delta^{\rm NQC}_{\rm extr}$ is instead the difference between the NQC input values extracted from the NR waveform with the same resolution level (the highest) and different extrapolation order (i.e., $N = 2$ and $N = 3$).

We find it convenient to define a few variables that enter the fits below:

$$\chi_{33} = \chi_S \delta m + \chi_A, \tag{B1}$$

$$\chi_{21A} = \frac{\chi_S}{1 - 1.3\nu}\delta m + \chi_A, \tag{B2}$$

$$\chi_{44A} = (1 - 5\nu)\chi_S + \chi_A \delta_m, \tag{B3}$$

$$\chi_{21D} = \frac{\chi_S}{1 - 2\nu}\delta m + \chi_A, \tag{B4}$$

$$\chi_{44D} = (1 - 7\nu)\chi_S + \chi_A \delta_m, \tag{B5}$$

$$\chi = \chi_S + \chi_A \frac{\delta m}{1 - 2\nu}. \tag{B6}$$

We notice that the variables $\chi_{33}, \chi_{21A}, \chi_{21D}$ are by definition zero in the equal-mass, equal-spin limit. They are used for the fits of the amplitude (and its derivative) to guarantee that in this limit the modes with m odd vanish, since they have to satisfy the symmetry under rotation $\varphi_0 \to \varphi_0 + \pi$.

1. Amplitude's fits

$$\frac{|h^{\rm NR}_{33}(t^{33}_{\rm match})|}{\nu} = |(0.101092 - 0.470410\nu + 1.073546\nu^2)\chi_{33} + \delta m(0.563658 - 0.054609\nu + 2.309370\nu^2 + 0.029813\chi^2_{33} - 0.0968810\nu\chi^2_{33})|, \tag{B7}$$

$$\frac{|h^{\rm NR}_{21}(t^{21}_{\rm match})|}{\nu} = |\delta m(-0.428179 + 0.113789\nu - 0.773677\nu^2 - 0.0101951\chi_{21A} + 0.0470041\chi^2_{21A} - 0.0932613\chi^2_{21A}\nu) + \chi_{21A}(0.292567 - 0.197103\nu) + \delta m 0.0168769\chi^3_{21A}|, \tag{B8}$$

$$\frac{|h^{\rm NR}_{44}(t^{44}_{\rm match})|}{\nu} = 0.264658 + 0.0675842\chi_{44A} + 0.029251\chi^2_{44A} + (-0.565825 - 0.866746\chi_{44A} + 0.00523419\chi^2_{44A})\nu + (-2.50083 + 6.88077\chi_{44A} - 1.02347\chi^2_{44A})\nu^2 + (7.69745 - 16.5515\chi_{44A})\nu^3, \tag{B9}$$

$$\frac{|h^{\rm NR}_{55}(t^{55}_{\rm match})|}{\nu} = |0.128621\delta m - 0.474201\delta m\nu + 1.0833\delta m\nu^2 + 0.0322784\chi_{33} - 0.134511\chi_{33}\nu + 0.0990202\chi_{33}\nu^2| \tag{B10}$$

2. Amplitude–first-derivative's fits

$$\frac{1}{\nu}\frac{d|h_{33}^{\rm NR}(t)|}{dt}\bigg|_{t=t_{\rm match}^{33}} = \delta m(-0.00309944 + 0.0100765\nu)\chi_{33}^2 + 0.00163096\sqrt{\delta m^2(8.81166 + 104.478\nu) + \delta m(-5.35204 + 49.6862\nu)\chi_{33} + \chi_{33}^2}, \tag{B11}$$

$$\frac{1}{\nu}\frac{d|h_{21}^{\rm NR}(t)|}{dt}\bigg|_{t=t_{\rm match}^{21}} = \delta m(0.00714753 - 0.0356440\nu) + 0.00801714|\chi_{21D}| - \delta m(0.787561 + 1.61127\nu + 11.30606\nu^2) + \delta m(-0.00877851 + 0.0305467\nu)\chi_{21D}, \tag{B12}$$

$$\frac{1}{\nu}\frac{d|h_{44}^{\rm NR}(t)|}{dt}\bigg|_{t=t_{\rm match}^{44}} = 0.00434759 - 0.00146122\chi_{44D} - 0.00242805\chi_{44D}^2 + (0.0233207 - 0.0224068\chi_{44D} + 0.0114271\chi_{44D}^2)\nu + (-0.460545 + 0.433527\chi_{44D})\nu^2 + (1.27963 - 1.24001\chi_{44D})\nu^3, \tag{B13}$$

$$\frac{1}{\nu}\frac{d|h_{55}^{\rm NR}(t)|}{dt}\bigg|_{t=t_{\rm match}^{55}} = \delta m(-0.0083898 + 0.0467835\nu) + \delta m(-0.00136056 + 0.00430271\nu)\chi_{33} + \delta m(-0.00114121 + 0.00185904\nu)\chi_{55}^2 + 0.000294422|\delta m(37.1113 - 157.799\nu) + \chi_{55}|. \tag{B14}$$

3. Amplitude–second-derivative's fits

$$\frac{1}{\nu}\frac{d^2|h_{33}^{\rm NR}(t)|}{dt^2}\bigg|_{t=t_{\rm match}^{33}} = \delta m(0.000960569 - 0.000190807\nu)\chi_{33} - 0.000156238|\delta m(4.67666 + 79.2019\nu - 1097.41\nu^2 + 6512.96\nu^3 - 13263.4\nu^4) + \chi_{33}|, \tag{B15}$$

$$\frac{1}{\nu}\frac{d^2|h_{21}^{\rm NR}(t)|}{dt^2}\bigg|_{t=t_{\rm match}^{21}} = 0.000371322\delta m - |\delta m(-0.000365087 - 0.00305417\nu) + \delta m(-0.000630623 - 0.000868048\nu + 0.0223062\nu^2)\chi_{21D}^2 + 0.000340243\chi_{21D}^3 + 0.000283985\delta m\chi_{21D}|, \tag{B16}$$

$$\frac{1}{\nu}\frac{d^2|h_{44}^{\rm NR}(t)|}{dt^2}\bigg|_{t=t_{\rm match}^{44}} = -0.000301723 + 0.000321595\chi + (0.00628305 + 0.00115988\chi)\nu + (-0.0814352 - 0.0138195\chi)\nu^2 + (0.226849 + 0.0327575\chi)\nu^3, \tag{B17}$$

$$\frac{1}{\nu}\frac{d^2|h_{55}^{\rm NR}(t)|}{dt^2}\bigg|_{t=t_{\rm match}^{55}} = \delta m(0.000127272 + 0.000321167\nu) + \delta m(-0.0000662168 + 0.000328855\nu)\chi_{33} + (-0.0000582462 + 0.000139443\nu)\chi_{33}^2. \tag{B18}$$

4. Frequency and frequency-derivative fits

$$\omega_{33}^{\rm NR}(t_{\rm match}^{33}) = 0.397395 + 0.164193\chi + 0.163553\chi^2 + 0.0614016\chi^3 + (0.699506 - 0.362674\chi - 0.977547\chi^2)\nu + (-0.345533 + 0.319523\chi + 1.93342\chi^2)\nu^2, \tag{B19}$$

$$\omega_{21}^{\rm NR}(t_{\rm match}^{21}) = 0.174319 + 0.0535087\chi + 0.0302288\chi^2 + (0.193894 - 0.184602\chi - 0.112222\chi^2)\nu + (0.167006 + 0.218731\chi)\nu^2, \tag{B20}$$

$$\omega_{44}^{\rm NR}(t_{\rm match}^{44}) = 0.538936 + 0.166352\chi + 0.207539\chi^2 + 0.152681\chi^3 + (0.76174 + 0.00958786\chi - 1.3023\chi^2 - 0.556275\chi^3)\nu + (0.967515 - 0.220593\chi + 2.6781\chi^2)\nu^2 - 4.89538\nu^3, \tag{B21}$$

$$\omega_{55}^{\rm NR}(t_{\rm match}^{55}) = 0.643755 + 0.223155\chi + 0.295689\chi^2 + 0.173278\chi^3 + (-0.470178 - 0.392901\chi - 2.26534\chi^2 - 0.5513\chi^3)\nu + (2.31148 + 0.882934\chi + 5.8176\chi^2)\nu^2. \tag{B22}$$

$$\dot{\omega}_{33}^{\rm NR}(t_{\rm match}^{33}) = 0.0103372 - 0.00530678\chi^2 - 0.00508793\chi^3 + (0.0277356 + 0.0188642\chi + 0.0217545\chi^2 + 0.0178548\chi^3)\nu + (0.0180842 - 0.0820427\chi)\nu^2, \tag{B23}$$

$$\dot{\omega}_{21}^{\rm NR}(t_{\rm match}^{21}) = 0.00709874 - 0.00177519\chi - 0.00356273\chi^2 - 0.0019021\chi^3 + (0.0248168 + 0.00424406\chi + 0.0147181\chi^2)\nu + (-0.050429 - 0.0319965\chi)\nu^2, \tag{B24}$$

$$\dot{\omega}_{44}^{\rm NR}(t_{\rm match}^{44}) = 0.0139979 - 0.00511782\chi - 0.00738743\chi^2 + (0.0528489 + 0.016323\chi + 0.0253907\chi^2)\nu + (-0.0652999 + 0.0578289\chi)\nu^2, \tag{B25}$$

$$\dot{\omega}_{55}^{\rm NR}(t_{\rm match}^{55}) = 0.0176343 - 0.000249257\chi - 0.0092404\chi^2 - 0.00790783\chi^3 + (-0.13660 + 0.0561378\chi + 0.164063\chi^2 + 0.0773623\chi^3)\nu + (0.987589 - 0.313921\chi - 0.592615\chi^2)\nu^2 - 1.694335\nu^3. \tag{B26}$$

APPENDIX C: FITS FOR AMPLITUDE AND PHASE OF MERGER-RINGDOWN MODEL

For these fits we apply the same selection of the NR waveforms discussed for the fits of the input values for the NQC. In particular, in performing the fits for the amplitude (phase) of the merger-ringdown signal, we weigh the contribution of the values extracted from every NR waveform with the same weight used for the NQC input value of the amplitude (frequency). It should be noted that in some cases, especially in the ringdown, the NR error in the (4,4) and (5,5) modes limits our ability to accurately model this part of the waveform (see Fig. 13).

$$c_{1,f}^{33} = 0.0763873 + 0.254345\nu - 1.08927\nu^2 - 0.0309934\chi + 0.251688\nu\chi - 0.798091\nu^2\chi, \tag{C1}$$

$$c_{2,f}^{33} = -0.832529 + 2.76799\nu - 7.02815\nu^2 - 0.59888\chi + 5.90437\nu\chi - 18.2326\nu^2\chi, \tag{C2}$$

$$c_{1,f}^{21} = 0.0778033 + 0.24091\nu - 0.745633\nu^2 - 0.0507064\chi + 0.385826\nu\chi - 0.969553\nu^2\chi, \tag{C3}$$

$$c_{2,f}^{21} = -1.24519 + 6.1342\nu - 14.6725\nu^2 - 1.19579\chi + 15.667\nu\chi - 44.4198\nu^2\chi, \tag{C4}$$

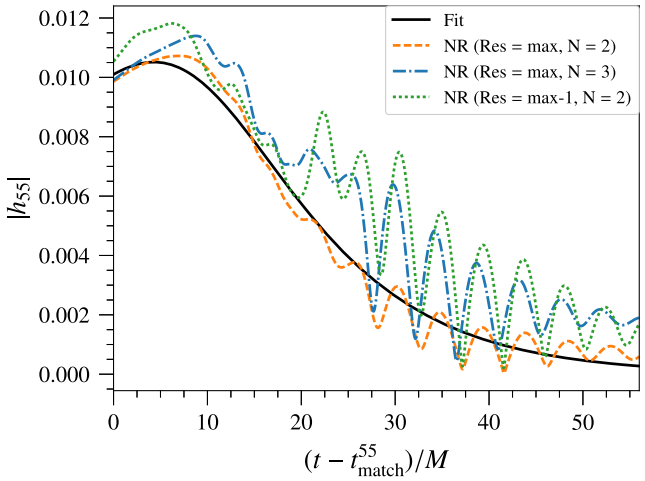

FIG. 13. Amplitudes of the (5,5) NR mode of the simulation `SXS:BBH:0065` ($q = 8, \chi_1 = 0.5, \chi_2 = 0$) for extraction order $N = 2$ and highest resolution (dashed orange), extraction order $N = 3$ and highest resolution (dotted-dashed blue), extraction order $N = 2$ and second highest resolution (dotted green). In solid black we show the result of the fit of the merger-ringdown signal used in the `SEOBNRv4HM` model.

$$c_{1,f}^{44} = -0.0639271 + 0.345195\nu - 1.76435\nu^2 - 0.0364617\chi + 1.27774\nu\chi - 14.8253\nu^2\chi + 40.6714\nu^3\chi, \quad \text{(C5)}$$

$$c_{2,f}^{44} = 0.781328 - 5.1869\nu + 14.0264\nu^2 + 0.809471\chi - 5.38343\nu\chi + 0.105163\nu^2\chi + 46.9784\nu^3\chi, \quad \text{(C6)}$$

$$c_{1,f}^{55} = -0.0670461 - 0.247549\nu + 0.758804\nu^2 + 0.0219059\chi - 0.0943771\nu\chi + 0.435777\nu^2\chi, \quad \text{(C7)}$$

$$c_{2,f}^{55} = 1.67634 - 5.60456\nu + 16.7513\nu^2 + 0.49257\chi - 6.2091\nu\chi + 16.7785\nu^2\chi. \quad \text{(C8)}$$

$$d_{1,f}^{33} = 0.110853 + 0.99998\nu - 3.39833\nu^2 + 0.0189591\chi - 0.72915\nu\chi + 2.5192\nu^2\chi, \quad \text{(C9)}$$

$$d_{2,f}^{33} = 2.78252 - 7.84474\nu + 27.181\nu^2 + 2.87968\chi - 34.767\nu\chi + 127.139\nu^2\chi, \quad \text{(C10)}$$

$$d_{1,f}^{21} = 0.156014 + 0.0233469\nu + 0.153266\nu^2 + 0.1022\chi - 0.943531\nu\chi + 1.79791\nu^2\chi, \quad \text{(C11)}$$

$$d_{2,f}^{21} = 2.78863 - 0.814541\nu + 5.54934\nu^2 + 4.2929\chi - 15.938\nu\chi + 12.6498\nu^2\chi, \quad \text{(C12)}$$

$$d_{1,f}^{44} = 0.11499 + 1.61265\nu - 6.2559\nu^2 + 0.00838952\chi - 0.806998\nu\chi + 7.59565\nu^2\chi - 19.3237\nu^3\chi, \quad \text{(C13)}$$

$$d_{2,f}^{44} = 3.11182 + 15.8853\nu - 79.6493\nu^2 + 5.39934\chi - 87.9242\nu\chi + 657.716\nu^2\chi - 1555.3\nu^3\chi, \quad \text{(C14)}$$

$$d_{1,f}^{55} = 0.164654 - 0.191845\nu + 0.333284\nu^2 - 0.0265748\chi - 0.0551962\nu\chi + 0.319427\nu^2\chi, \quad \text{(C15)}$$

$$d_{2,f}^{55} = 11.1024 - 58.6058\nu + 176.606\nu^2 + 6.01511\chi - 81.6803\nu\chi + 266.473\nu^2\chi. \quad \text{(C16)}$$

APPENDIX D: FITS FOR THE PHASE DIFFERENCE BETWEEN HIGHER-ORDER MODES AND (2,2) MODE AT THE MATCHING POINT $t_{\rm match}^{\ell m}$

The relations between $\phi_{\rm match}^{\ell m}$ [i.e., the phase of the (ℓ, m) modes computed at $t_{\rm match}^{\ell m}$] and $\phi_{\rm match}^{22}$ are

$$\Delta\phi_{\rm match}^{33} \equiv \phi_{\rm match}^{33} - \frac{3}{2}(\phi_{\rm match}^{22} - \pi) \pmod{\pi}, \quad \text{(D1)}$$

$$\Delta\phi_{\rm match}^{21} \equiv \phi_{\rm match}^{21} - \frac{1}{2}(\phi_{\rm match}^{22} - \pi) \pmod{\pi}, \quad \text{(D2)}$$

$$\Delta\phi_{\rm match}^{44} \equiv \phi_{\rm match}^{44} - (2\phi_{\rm match}^{22} - \pi) \pmod{2\pi}, \quad \text{(D3)}$$

$$\Delta\phi_{\rm match}^{55} \equiv \phi_{\rm match}^{55} - \frac{1}{2}(5\phi_{\rm match}^{22} - \pi) \pmod{\pi}, \quad \text{(D4)}$$

where the RHS is the scaling of the phase at leading PN order, and the LHS is the deviation from the latter, computed at $t_{\rm match}^{\ell m}$. The term $\Delta\phi_{\rm match}^{\ell m}$ is extracted from each NR and Teukolsky–equation-based waveforms in our catalog and then fitted as a function of (ν, χ). We find

$$\Delta\phi_{\rm match}^{33} = 3.20275 - 1.47295\sqrt{\delta m} + 1.21021\delta m - 0.203442\chi + \delta m^2(-0.0284949 - 0.217949\chi)\chi \pmod{\pi}, \quad \text{(D5)}$$

$$\Delta\phi_{\rm match}^{21} = 2.28855 + 0.200895\delta m - 0.0403123\chi + \delta m^2(-0.0331133 - 0.0424056\chi - 0.0244154\chi^2) \pmod{\pi}, \quad \text{(D6)}$$

$$\Delta\phi_{\rm match}^{44} = 5.89306 + \nu^2(-36.7321 - 21.9229\chi) - 0.499652\chi - 0.292006\chi^2 + \nu^3(160.102 + 67.0793\chi) + \nu(2.48143 + 3.26618\chi + 1.38065\chi^2) \pmod{2\pi}, \quad \text{(D7)}$$

$$\Delta\phi_{\rm match}^{55} = 3.61933 - 1.52671\delta m - 0.172907\chi + \delta m^2(0.72564 - 0.44462\chi - 0.528597\chi^2) \pmod{\pi}. \quad \text{(D8)}$$

The error on the phase of each mode caused by the fit of $\Delta\phi_{\rm match}^{\ell m}$ is on average of the order of 0.05 rad.

APPENDIX E: FITS FOR TIME DIFFERENCE BETWEEN MODES' AMPLITUDE PEAKS

As originally observed in Refs. [45,53], gravitational modes peak at different times ($t_{\rm peak}^{\ell m}$) with respect to the dominant (2,2) mode. Using the NR catalog at our disposal, we fit the times shifts $\Delta t_{\ell m} \equiv t_{\rm peak}^{\ell m} - t_{\rm peak}^{22}$ as function of ν and $\chi_{\rm eff} = (m_1\chi_1 + m_2\chi_2)/M$. We find

$$\Delta t_{33} = 4.20646 + 4.215\chi_{\rm eff} + 2.12487\chi_{\rm eff}^2 + (-10.9615 + 5.20758a)\nu + (53.3674 - 65.0849a)\nu^2, \quad \text{(E1)}$$

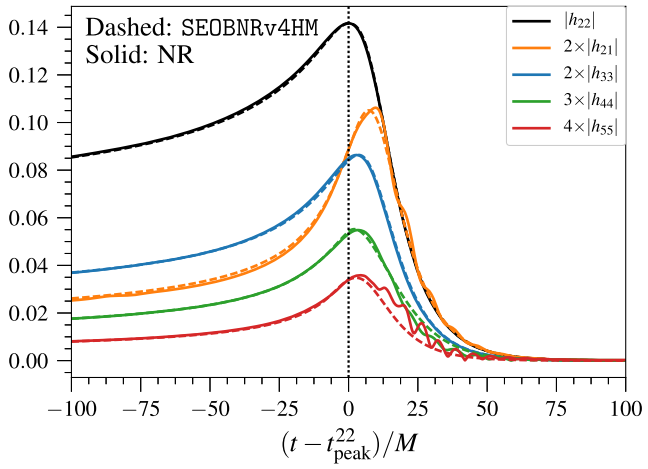

FIG. 14. Amplitudes of different modes for the SEOBNRv4HM (dashed) and NR (solid) waveforms with $(q=8,\chi_1=-0.5,\chi_2=0)$ (SXS:BBH:0064) versus time. The time origin corresponds to the (2,2) mode's peak.

$$\Delta t_{21} = 12.892 + 1.14433\chi_{\rm eff} + 1.12146\chi^2_{\rm eff} + (-61.1508 - 96.0301\chi_{\rm eff} - 85.4386\chi^2_{\rm eff})\nu + (144.497 + 366.374\chi_{\rm eff} + 322.06\chi^2_{\rm eff})\nu^2, \quad \text{(E2)}$$

$$\Delta t_{44} = 7.49641 + 6.7245\chi_{\rm eff} + 3.11618\chi^2_{\rm eff} + (-48.5578 - 78.8077\chi_{\rm eff} - 92.1608\chi^2_{\rm eff})\nu + (91.483 + 231.917\chi_{\rm eff} + 388.074\chi^2_{\rm eff})\nu^2, \quad \text{(E3)}$$

$$\Delta t_{55} = 10.031 + 5.80884\chi_{\rm eff} + (-103.252 - 75.8935\chi_{\rm eff})\nu + (366.57 + 282.552\chi_{\rm eff})\nu^2. \quad \text{(E4)}$$

The above expressions could be employed in building phenomenological models for the ringdown signal when multipole modes are present [65]. We notice that these fits are not used for building SEOBNRv4HM waveforms, whose merger-ringdown model is constructed through Eqs. (4.19)–(4.21), starting from $t^{\ell m}_{\rm match}$ in Eq. (4.3). The merger-ringdown SEOBNRv4HM waveforms reproduce the time shifts $\Delta t_{\ell m}$ between the NR modes' amplitude peaks by construction, as it can be seen in Fig. 14 for a particular binary configuration.

We emphasize that while in the EOBNRv2HM model [45] the merger-ringdown attachment was done at each modes' peak time, in SEOBNRv4HM we do it at the (2,2) mode's peak for all modes except the (5,5) mode. We make this change here because typically $\Delta t_{\ell m} = t^{\ell m}_{\rm peak} - t^{22}_{\rm peak} > 0$, and at these late times we find that for some binary configurations either the EOB dynamics becomes unreliable or the error in the NR waveforms is too large and prevents us to accurately extract the input values for the NQC conditions [i.e., Eqs. (4.14)–(4.18)].

APPENDIX F: NUMERICAL-RELATIVITY CATALOG

In the tables below we list the binary configurations of the NR simulations used to build and test the SEOBNRv4HM waveform model. The NR waveforms were produced with the (pseudo) Spectral Einstein code (SpEC) of the Simulating eXtreme Spacetimes (SXS) project and the Einstein Toolkit (ET) code. In particular, we list the mass ratio q, the dimensionless spins $\chi_{1,2}$, the eccentricity e, the initial frequency ω_{22} of the dominant $(\ell,m)=(2,2)$ mode and the number of orbits $N_{\rm orb}$ up to the waveform peak.

In Fig. 15 we show the coverage of NR and BH-perturbation-theory waveforms when projected on the binary's parameters ν and $\chi_{\rm eff}=(\chi_1 m_1+\chi_2 m_2)/M$. We highlight four regions. In the first region $1\le q\le 3$ there is a large number of configurations with both BHs carrying spin. The spins magnitude are as high as $\chi_{1,2}=0.99$ in the equal-mass limit, while they are limited to $\chi_{1,2}=0.85$ for $q=3$. The second region is between $3<q\le 8$, and most of the simulations have spins only on the heavier BH. The values of the spin of the heavier BH span in the region $-0.8\le\chi_1\le 0.85$. The third region is between $8<q\le 10$ and it includes only nonspinning waveforms. Finally, the fourth region covers 13 waveforms computed solving the Teukolsky equation in the framework of BH perturbation theory [53,54]. They have $q=10^3$ and dimensionless spins values in the range $-0.99\le\chi\le 0.99$.

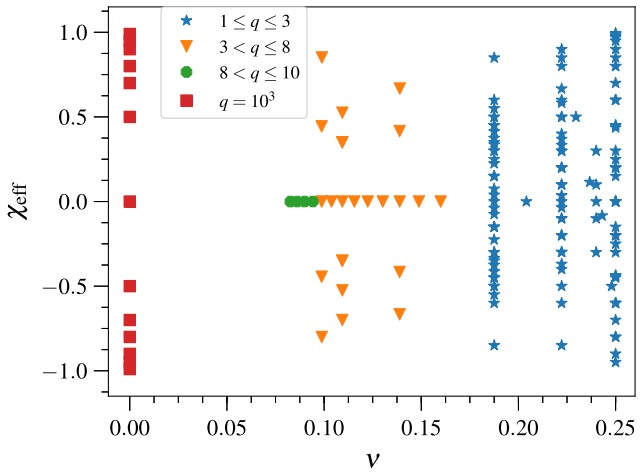

FIG. 15. 2D projection of the 3D parameter space of the NR and BH-perturbation-theory waveforms used to build the SEOBNRv4HM model. The x-axis is ν and the y-axis is the effective spin $\chi_{\rm eff}=(\chi_1 m_1+\chi_2 m_2)/M$. In the legend we highlight four different regions of coverage, as discussed in the text.

1. SXS and ET waveform produced for testing SEOBNRv4 (Ref. [27])

ID	q	χ_1	χ_2	e	$M\omega_{22}$	$N_{\rm orb}$
SXS:BBH:0610	1.2	−0.50	−0.50	7.4×10^{-5}	0.01872	12.1
SXS:BBH:0611	1.4	−0.50	+0.50	6.0×10^{-4}	0.02033	12.5
SXS:BBH:0612	1.6	+0.50	−0.50	3.7×10^{-4}	0.02156	12.8
SXS:BBH:0613	1.8	+0.50	+0.50	1.8×10^{-4}	0.02383	13.1
SXS:BBH:0614	2.0	+0.75	−0.50	6.7×10^{-4}	0.02355	13.1
SXS:BBH:0615	2.0	+0.75	+0.00	7.0×10^{-4}	0.02401	13.3
SXS:BBH:0616	2.0	+0.75	+0.50	8.0×10^{-4}	0.02475	13.3
SXS:BBH:0617	2.0	+0.50	+0.75	7.8×10^{-4}	0.02342	13.1
SXS:BBH:0618	2.0	+0.80	+0.80	5.9×10^{-4}	0.02578	13.4
SXS:BBH:0620	5.0	−0.80	+0.00	3.4×10^{-3}	0.02527	8.2
SXS:BBH:0621	7.0	−0.80	+0.00	3.2×10^{-3}	0.02784	7.1
SXS:BBH:0619	2.0	+0.90	+0.90	2.9×10^{-4}	0.02520	13.5
ET:AEI:0001	5.0	+0.80	+0.00	9.2×10^{-4}	0.03077	10.5
ET:AEI:0002	7.0	+0.80	+0.00	6.1×10^{-4}	0.03503	10.4
ET:AEI:0004	8.0	+0.85	+0.85	3.0×10^{-3}	0.04368	7.4

2. SXS waveforms from Ref. [60]

ID	q	χ_1	χ_2	e	$M\omega_{22}$	$N_{\rm orb}$
SXS:BBH:0004	1.0	−0.50	+0.00	3.7×10^{-4}	0.01151	30.2
SXS:BBH:0005	1.0	+0.50	+0.00	2.5×10^{-4}	0.01227	30.2
SXS:BBH:0007	1.5	+0.00	+0.00	4.2×10^{-4}	0.01229	29.1
SXS:BBH:0013	1.5	+0.50	+0.00	1.4×10^{-4}	0.01444	23.8
SXS:BBH:0016	1.5	−0.50	+0.00	4.2×10^{-4}	0.01149	30.7
SXS:BBH:0019	1.5	−0.50	+0.50	7.6×10^{-5}	0.01460	20.4
SXS:BBH:0025	1.5	+0.50	−0.50	7.6×10^{-5}	0.01456	22.4
SXS:BBH:0030	3.0	+0.00	+0.00	2.0×10^{-3}	0.01775	18.2
SXS:BBH:0036	3.0	−0.50	+0.00	5.1×10^{-4}	0.01226	31.7
SXS:BBH:0045	3.0	+0.50	−0.50	6.4×10^{-4}	0.01748	21.0
SXS:BBH:0046	3.0	−0.50	−0.50	2.6×10^{-4}	0.01771	14.4
SXS:BBH:0047	3.0	+0.50	+0.50	4.7×10^{-4}	0.01743	22.7
SXS:BBH:0056	5.0	+0.00	+0.00	4.9×10^{-4}	0.01589	28.8
SXS:BBH:0060	5.0	−0.50	+0.00	3.4×10^{-3}	0.01608	23.2
SXS:BBH:0061	5.0	+0.50	+0.00	4.2×10^{-3}	0.01578	34.5
SXS:BBH:0063	8.0	+0.00	+0.00	2.8×10^{-4}	0.01938	25.8
SXS:BBH:0064	8.0	−0.50	+0.00	4.9×10^{-4}	0.01968	19.2
SXS:BBH:0065	8.0	+0.50	+0.00	3.7×10^{-3}	0.01887	34.0
SXS:BBH:0148	1.0	−0.44	−0.44	2.0×10^{-5}	0.01634	15.5
SXS:BBH:0149	1.0	−0.20	−0.20	1.8×10^{-4}	0.01614	17.1
SXS:BBH:0150	1.0	+0.20	+0.20	2.9×10^{-4}	0.01591	19.8
SXS:BBH:0151	1.0	−0.60	−0.60	2.5×10^{-4}	0.01575	14.5
SXS:BBH:0152	1.0	+0.60	+0.60	4.3×10^{-4}	0.01553	22.6
SXS:BBH:0153	1.0	+0.85	+0.85	8.3×10^{-4}	0.01539	24.5
SXS:BBH:0154	1.0	−0.80	−0.80	3.3×10^{-4}	0.01605	13.2
SXS:BBH:0155	1.0	+0.80	+0.80	4.7×10^{-4}	0.01543	24.1
SXS:BBH:0156	1.0	−0.95	−0.95	5.4×10^{-4}	0.01643	12.4
SXS:BBH:0157	1.0	+0.95	+0.95	1.4×10^{-4}	0.01535	25.2
SXS:BBH:0158	1.0	+0.97	+0.97	7.9×10^{-4}	0.01565	25.3
SXS:BBH:0159	1.0	−0.90	−0.90	5.6×10^{-4}	0.01588	12.7
SXS:BBH:0160	1.0	+0.90	+0.90	4.2×10^{-4}	0.01538	24.8
SXS:BBH:0166	6.0	+0.00	+0.00	4.4×10^{-5}	0.01940	21.6
SXS:BBH:0167	4.0	+0.00	+0.00	9.9×10^{-5}	0.02054	15.6
SXS:BBH:0169	2.0	+0.00	+0.00	1.2×10^{-4}	0.01799	15.7
SXS:BBH:0170	1.0	+0.44	+0.44	1.3×10^{-4}	0.00842	15.5
SXS:BBH:0172	1.0	+0.98	+0.98	7.8×10^{-4}	0.01540	25.4
SXS:BBH:0174	3.0	+0.50	+0.00	2.9×10^{-4}	0.01337	35.5
SXS:BBH:0180	1.0	+0.00	+0.00	5.1×10^{-5}	0.01227	28.2

3. SXS waveforms from Refs. [57–59]

ID	q	χ_1	χ_2	e	$M\omega_{22}$	$N_{\rm orb}$
SXS:BBH:0177	1.0	+0.99	+0.99	1.3×10^{-3}	0.01543	25.4
SXS:BBH:0178	1.0	+0.99	+0.99	8.6×10^{-4}	0.01570	25.4
SXS:BBH:0202	7.0	+0.60	+0.00	9.0×10^{-5}	0.01324	62.1
SXS:BBH:0203	7.0	+0.40	+0.00	1.4×10^{-5}	0.01322	58.5
SXS:BBH:0204	7.0	+0.40	+0.00	1.7×10^{-4}	0.01044	88.4
SXS:BBH:0205	7.0	−0.40	+0.00	7.0×10^{-5}	0.01325	44.9
SXS:BBH:0206	7.0	−0.40	+0.00	1.6×10^{-4}	0.01037	73.2
SXS:BBH:0207	7.0	−0.60	+0.00	1.7×10^{-4}	0.01423	36.1
SXS:BBH:0306	1.3	+0.96	−0.90	1.5×10^{-3}	0.02098	12.6

4. SXS waveforms from Ref. [50]

ID	q	χ_1	χ_2	e	$M\omega_{22}$	$N_{\rm orb}$
SXS:BBH:0290	3.0	+0.60	+0.40	9.0×10^{-5}	0.01758	24.2
SXS:BBH:0291	3.0	+0.60	+0.60	5.0×10^{-5}	0.01764	24.5
SXS:BBH:0289	3.0	+0.60	+0.00	2.3×10^{-4}	0.01711	23.8
SXS:BBH:0285	3.0	+0.40	+0.60	1.6×10^{-4}	0.01732	23.8
SXS:BBH:0261	3.0	−0.73	+0.85	1.0×10^{-4}	0.01490	21.5
SXS:BBH:0293	3.0	+0.85	+0.85	9.0×10^{-5}	0.01813	25.6
SXS:BBH:0280	3.0	+0.27	+0.85	9.7×10^{-5}	0.01707	23.6
SXS:BBH:0257	2.0	+0.85	+0.85	1.1×10^{-4}	0.01633	24.8
SXS:BBH:0279	3.0	+0.23	−0.85	6.0×10^{-5}	0.01629	22.6
SXS:BBH:0274	3.0	−0.23	+0.85	1.6×10^{-4}	0.01603	22.4
SXS:BBH:0258	2.0	+0.87	−0.85	1.8×10^{-4}	0.01612	22.8
SXS:BBH:0248	2.0	+0.13	+0.85	7.0×10^{-5}	0.01552	23.2
SXS:BBH:0232	1.0	+0.90	+0.50	2.8×10^{-4}	0.01558	23.9
SXS:BBH:0229	1.0	+0.65	+0.25	3.1×10^{-4}	0.01488	23.1
SXS:BBH:0231	1.0	+0.90	+0.00	1.0×10^{-4}	0.01487	23.1
SXS:BBH:0239	2.0	−0.37	+0.85	9.1×10^{-5}	0.01478	22.2
SXS:BBH:0252	2.0	+0.37	−0.85	3.8×10^{-4}	0.01488	22.5
SXS:BBH:0219	1.0	−0.50	+0.90	3.3×10^{-4}	0.01484	22.4
SXS:BBH:0211	1.0	−0.90	+0.90	2.6×10^{-4}	0.01411	22.3
SXS:BBH:0233	2.0	−0.87	+0.85	6.0×10^{-5}	0.01423	22.0
SXS:BBH:0243	2.0	−0.13	−0.85	1.8×10^{-4}	0.01378	23.3
SXS:BBH:0214	1.0	−0.62	−0.25	1.9×10^{-4}	0.01264	24.4
SXS:BBH:0209	1.0	−0.90	−0.50	1.7×10^{-4}	0.01137	27.0

(Continued)

ID	q	χ_1	χ_2	e	$M\omega_{22}$	$N_{\rm orb}$
SXS:BBH:0226	1.0	+0.50	−0.90	2.4×10^{-4}	0.01340	22.9
SXS:BBH:0286	3.0	+0.50	+0.50	8.0×10^{-5}	0.01693	24.1
SXS:BBH:0253	2.0	+0.50	+0.50	6.7×10^{-5}	0.01397	28.8
SXS:BBH:0267	3.0	−0.50	−0.50	5.6×10^{-5}	0.01410	23.4
SXS:BBH:0218	1.0	−0.50	+0.50	7.8×10^{-5}	0.01217	29.1
SXS:BBH:0238	2.0	−0.50	−0.50	6.9×10^{-5}	0.01126	32.0
SXS:BBH:0288	3.0	+0.60	−0.40	1.9×10^{-4}	0.01729	23.5
SXS:BBH:0287	3.0	+0.60	−0.60	7.0×10^{-5}	0.01684	23.5
SXS:BBH:0283	3.0	+0.30	+0.30	7.6×10^{-5}	0.01646	23.5
SXS:BBH:0282	3.0	+0.30	+0.00	7.5×10^{-5}	0.01629	23.3
SXS:BBH:0281	3.0	+0.30	−0.30	6.7×10^{-5}	0.01618	23.2
SXS:BBH:0277	3.0	+0.00	+0.30	7.0×10^{-5}	0.01595	22.9
SXS:BBH:0284	3.0	+0.40	−0.60	1.5×10^{-4}	0.01656	22.8
SXS:BBH:0278	3.0	+0.00	+0.60	2.1×10^{-4}	0.01623	22.8
SXS:BBH:0256	2.0	+0.60	+0.60	7.8×10^{-5}	0.01598	23.9
SXS:BBH:0230	1.0	+0.80	+0.80	1.3×10^{-4}	0.01542	24.2
SXS:BBH:0255	2.0	+0.60	+0.00	4.0×10^{-5}	0.01580	23.3
SXS:BBH:0276	3.0	+0.00	−0.30	6.7×10^{-5}	0.01559	23.0
SXS:BBH:0251	2.0	+0.30	+0.30	7.5×10^{-5}	0.01514	23.5
SXS:BBH:0250	2.0	+0.30	+0.00	7.5×10^{-5}	0.01503	23.2
SXS:BBH:0271	3.0	−0.30	+0.00	6.3×10^{-5}	0.01508	22.5
SXS:BBH:0249	2.0	+0.30	−0.30	7.2×10^{-5}	0.01478	23.2
SXS:BBH:0275	3.0	+0.00	−0.60	1.2×10^{-4}	0.01569	22.6
SXS:BBH:0254	2.0	+0.60	−0.60	6.0×10^{-5}	0.01541	22.9
SXS:BBH:0269	3.0	−0.40	+0.60	1.2×10^{-4}	0.01563	22.3
SXS:BBH:0225	1.0	+0.40	+0.80	3.5×10^{-4}	0.01536	23.5
SXS:BBH:0270	3.0	−0.30	−0.30	6.2×10^{-5}	0.01482	22.8
SXS:BBH:0245	2.0	+0.00	−0.30	6.8×10^{-5}	0.01441	23.0
SXS:BBH:0242	2.0	−0.30	+0.30	6.7×10^{-5}	0.01417	23.1
SXS:BBH:0223	1.0	+0.30	+0.00	6.7×10^{-5}	0.01402	23.3
SXS:BBH:0241	2.0	−0.30	+0.00	6.6×10^{-5}	0.01394	23.1
SXS:BBH:0240	2.0	−0.30	−0.30	6.4×10^{-5}	0.01359	23.5
SXS:BBH:0222	1.0	−0.30	+0.00	7.4×10^{-5}	0.01324	23.6
SXS:BBH:0228	1.0	+0.60	+0.60	3.2×10^{-4}	0.01543	23.5
SXS:BBH:0247	2.0	+0.00	+0.60	1.0×10^{-4}	0.01530	22.6
SXS:BBH:0263	3.0	−0.60	+0.60	1.9×10^{-4}	0.01526	22.0
SXS:BBH:0266	3.0	−0.60	+0.40	1.8×10^{-4}	0.01488	22.0
SXS:BBH:0227	1.0	+0.60	+0.00	3.1×10^{-4}	0.01452	23.1
SXS:BBH:0221	1.0	−0.40	+0.80	2.7×10^{-4}	0.01440	22.7
SXS:BBH:0237	2.0	−0.60	+0.60	6.1×10^{-5}	0.01433	22.6
SXS:BBH:0244	2.0	+0.00	−0.60	7.5×10^{-5}	0.01422	23.2
SXS:BBH:0217	1.0	−0.60	+0.60	1.5×10^{-4}	0.01421	22.7
SXS:BBH:0215	1.0	−0.60	−0.60	1.8×10^{-4}	0.01189	25.8
SXS:BBH:0262	3.0	−0.60	+0.00	2.0×10^{-4}	0.01473	22.5
SXS:BBH:0213	1.0	−0.80	+0.80	1.4×10^{-4}	0.01435	22.3
SXS:BBH:0265	3.0	−0.60	−0.40	9.0×10^{-5}	0.01422	23.4
SXS:BBH:0264	3.0	−0.60	−0.60	2.8×10^{-4}	0.01410	23.4
SXS:BBH:0224	1.0	+0.40	−0.80	2.5×10^{-4}	0.01361	22.9
SXS:BBH:0236	2.0	−0.60	+0.00	1.2×10^{-4}	0.01361	23.4
SXS:BBH:0216	1.0	−0.60	+0.00	2.6×10^{-4}	0.01300	23.6
SXS:BBH:0235	2.0	−0.60	−0.60	6.1×10^{-5}	0.01274	25.1
SXS:BBH:0220	1.0	−0.40	−0.80	1.0×10^{-4}	0.01195	25.7

(Table continued)

(Continued)

ID	q	χ_1	χ_2	e	$M\omega_{22}$	$N_{\rm orb}$
SXS:BBH:0212	1.0	−0.80	−0.80	2.4×10^{-4}	0.01087	28.6
SXS:BBH:0303	10.0	+0.00	+0.00	5.1×10^{-5}	0.02395	19.3
SXS:BBH:0300	8.5	+0.00	+0.00	5.7×10^{-5}	0.02311	18.7
SXS:BBH:0299	7.5	+0.00	+0.00	5.9×10^{-5}	0.02152	20.1
SXS:BBH:0298	7.0	+0.00	+0.00	6.1×10^{-5}	0.02130	19.7
SXS:BBH:0297	6.5	+0.00	+0.00	6.4×10^{-5}	0.02082	19.7
SXS:BBH:0296	5.5	+0.00	+0.00	5.2×10^{-5}	0.01668	27.9
SXS:BBH:0295	4.5	+0.00	+0.00	5.2×10^{-5}	0.01577	27.8
SXS:BBH:0259	2.5	+0.00	+0.00	5.9×10^{-5}	0.01346	28.6
SXS:BBH:0292	3.0	+0.73	−0.85	1.8×10^{-4}	0.01749	23.9
SXS:BBH:0268	3.0	−0.40	−0.60	1.7×10^{-4}	0.01473	22.9
SXS:BBH:0234	2.0	−0.85	−0.85	1.4×10^{-4}	0.01147	27.8
SXS:BBH:0273	3.0	−0.27	−0.85	2.0×10^{-4}	0.01487	22.9
SXS:BBH:0210	1.0	−0.90	+0.00	1.8×10^{-4}	0.01248	24.3
SXS:BBH:0260	3.0	−0.85	−0.85	3.5×10^{-4}	0.01285	25.8
SXS:BBH:0302	9.5	+0.00	+0.00	6.0×10^{-5}	0.02366	19.1
SXS:BBH:0301	9.0	+0.00	+0.00	5.5×10^{-5}	0.02338	18.9
SXS:BBH:0272	3.0	−0.30	+0.30	6.4×10^{-5}	0.01521	22.7
SXS:BBH:0246	2.0	+0.00	+0.30	7.2×10^{-5}	0.01514	22.9

APPENDIX G: COMPARING THE NONSPINNING SEOBNRv4HM AND EOBNRv2HM MODELS

Here we compare the nonspinning limit of SEOBNRv4HM to its predecessor, the EOBNRv2HM model developed in 2011 [45], which is available in the LIGO Algorithm Library (LAL) and it has been used in Refs. [38,41,79] to assess the importance of higher-order modes in Advanced LIGO searches and parameter estimation. The model EOBNRv2HM was also used to search for intermediate binary black holes [105–108]). The EOBNRv2HM model includes the same higher-order modes as SEOBNRv4HM, that is (2,2), (2,1), (3,3), (4,4), (5,5). Given that the EOBNRv2HM model was calibrated against NR waveforms up to mass ratio $q = 6$, we decide to compare first the two models for a configuration with this mass ratio (SXS:BBH:0166). In Fig. 16 we show the unfaithfulness results for maximum, minimum, average and SNR-weighted average with respect to the angles $\iota_{\rm NR}, \varphi_{0\rm NR}, \kappa_{\rm NR}$ of the models against NR waveforms with the modes $(\ell \leq 5, m \neq 0)$. The unfaithfulness is shown as a function of total mass. The dashed (solid) lines represent the results for EOBNRv2HM (SEOBNRv4HM). The minimum of the unfaithfulness, reached for a face-on orientation, is different for the two models and it is smaller for the SEOBNRv4HM model. Since, for a face-on orientation, all the higher-order modes included in the two models are exactly zero because of the spherical harmonics, this difference is only due to a better modeling of the dominant $(\ell, m) = (2, 2)$ mode. This difference is very small and both models yield a minimum of the unfaithfulness much smaller than 1% in the total mass

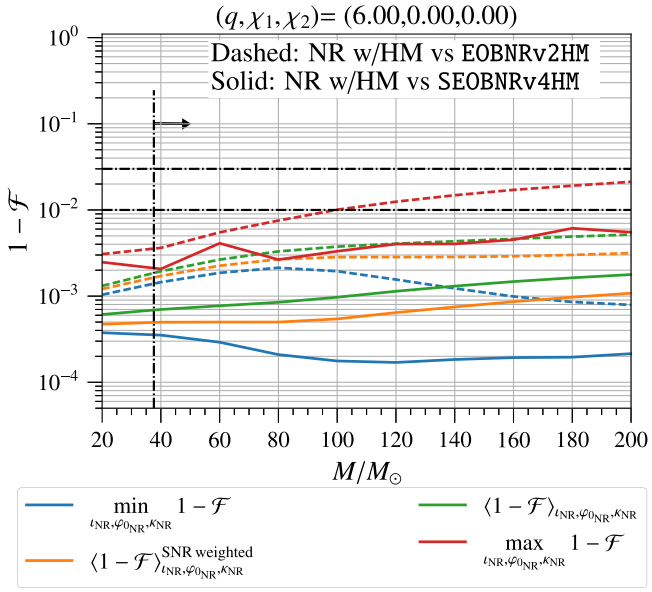

FIG. 16. Unfaithfulness $(1-\mathcal{F})$ in the mass range $20\ M_\odot \leq M \leq 200\ M_\odot$ for the configuration $(q=6, \chi_1=\chi_2=0)$. Dashed (plain) curves refer to results for EOBNRv2HM (SEOBNRv4HM). Plotted data as in Fig. 7.

range $20\ M_\odot \leq M \leq 200\ M_\odot$. The most important quantity to compare is the maximum of the unfaithfulness which is reached for an edge-on orientation, where the higher-order modes are more relevant. Also in this case the SEOBNRv4HM model has a lower unfaithfulness against the NR waveform with respect to the EOBNRv2HM model. In particular at a total mass of $M = 200\ M_\odot$ EOBNRv2HM returns a maximum unfaithfulness $(1-\mathcal{F}) \sim 2\%$, while the SEOBNRv4HM model only $(1-\mathcal{F}) \sim 0.6\%$. This means that also the higher-order modes are better modeled in SEOBNRv4HM with respect to EOBNRv2HM.

We find that the model SEOBNRv4HM returns smaller values of the unfaithfulness against the NR waveforms than the EOBNRv2HM model for every nonspinning configuration in our NR catalog with $q \leq 6$. A comparison between the two models for mass ratio higher than $q = 6$ is unfair because EOBNRv2HM is not calibrated in this region. However it is worth mentioning that for the numerical simulation with the largest mass ratio at our disposal $(q = 10)$ the average unfaithfulness of EOBNRv2HM is larger than that of SEOBNRv4HM, but still smaller than 1% in the mass range considered. For this configuration the value of the maximum of the unfaithfulness is $(1-\mathcal{F}) \sim 3.5\%$ for EOBNRv2HM at $M = 200\ M_\odot$, while is $(1-\mathcal{F}) \sim 2\%$ for SEOBNRv4HM.

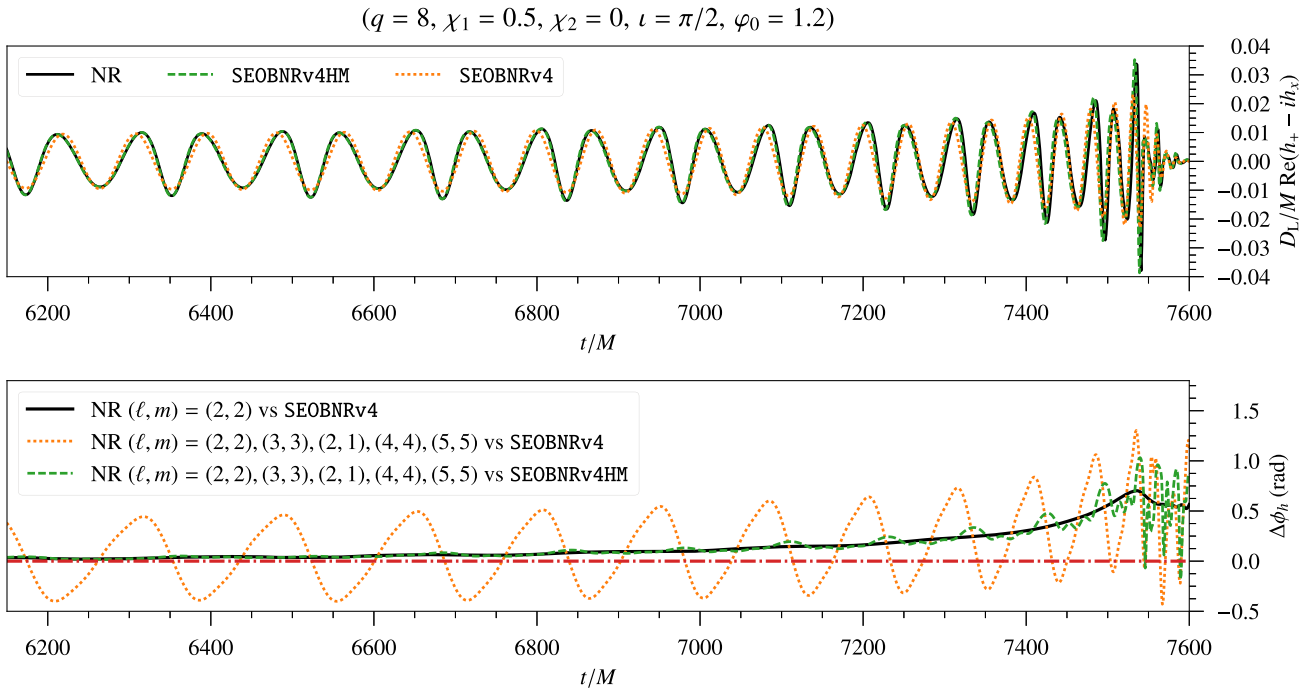

FIG. 17. Comparison between NR (solid black), SEOBNRv4HM (dashed green) and SEOBNRv4 (dotted yellow) waveforms in an edge-on orientation $(\iota = \pi/2, \varphi_0 = 1.2)$ for the NR simulation SXS:BBH:0065 $(q = 8, \chi_1 = 0.5, \chi_2 = 0)$. In the top panel is plotted the real part of the observer-frame's gravitational strain $h_+(\iota,\varphi_0;t) - ih_x(\iota,\varphi_0;t)$, while in the bottom panel the dephasing with the NR waveform $\Delta\phi_h$.The dotted-dashed red horizontal line in the bottom panel indicates zero dephasing with the NR waveform. Both SEOBNRv4 and SEOBNRv4HM waveforms are phase aligned and time shifted at low frequency using as alignment window $t_{\text{ini}} = 1000M$ and $t_{\text{fin}} = 3000M$.

APPENDIX H: COMPARING SEOBNRv4HM AND NUMERICAL-RELATIVITY WAVEFORMS IN TIME DOMAIN

The improvement in waveform modeling obtained by including higher-order modes, can also be seen from a direct comparison of NR waveforms to SEOBNRv4 and SEOBNRv4HM waveforms in time domain. We present this comparison in Fig. 17 for the simulation SXS:BBH:0065. We show the NR waveform with (2,2), (2,1), (3,3), (4,4), (5,5) modes (solid black), the SEOBNRv4HM (dashed green) and SEOBNRv4 (dotted yellow) waveforms in an edge-on orientation. The effect of neglecting higher-order modes results in an oscillatory phase difference (dotted yellow curve of the bottom panel in Fig. 17) around the mean dephasing due to the dominant (2,2) mode (solid black curve of the same panel). These oscillations in the dephasing are almost totally removed up to merger when we include higher-order modes (dashed green of the bottom panel in Fig. 17) where now the phase difference with the NR waveform is dominated again by the discrepancy of the (2,2) mode. The residual oscillations of the dashed green curve around the dephasing of the dominant (2,2) mode is due to the superposition of the different dephasing of the various higher-order modes. The effect of the inclusion of higher-order modes can be seen also in the amplitude of the waveform, in particular in the last five cycle of the waveform there is an evident amplitude difference between SEOBNRv4 and NR waveforms, which is not present when the SEOBNRv4HM waveform is used.

[1] J. Aasi *et al.* (LIGO Scientific), Classical Quantum Gravity **32**, 115012 (2015).
[2] B. P. Abbott *et al.* (Virgo, LIGO Scientific), Phys. Rev. Lett. **116**, 061102 (2016).
[3] B. P. Abbott *et al.* (Virgo, LIGO Scientific), Phys. Rev. Lett. **116**, 241103 (2016).
[4] B. P. Abbott *et al.* (VIRGO, LIGO Scientific), Phys. Rev. Lett. **118**, 221101 (2017).
[5] B. P. Abbott *et al.* (Virgo, LIGO Scientific), Astrophys. J. **851**, L35 (2017).
[6] B. P. Abbott *et al.* (Virgo, LIGO Scientific), Phys. Rev. Lett. **119**, 141101 (2017).
[7] F. Acernese *et al.* (VIRGO), Classical Quantum Gravity **32**, 024001 (2015).
[8] B. P. Abbott *et al.* (Virgo, LIGO Scientific), Phys. Rev. Lett. **119**, 161101 (2017).
[9] A. H. Nitz, T. Dent, T. Dal Canton, S. Fairhurst, and D. A. Brown, Astrophys. J. **849**, 118 (2017).
[10] J. Veitch *et al.*, Phys. Rev. D **91**, 042003 (2015).
[11] S. A. Usman *et al.*, Classical Quantum Gravity **33**, 215004 (2016).
[12] T. Dal Canton *et al.*, Phys. Rev. D **90**, 082004 (2014).
[13] K. Cannon *et al.*, Astrophys. J. **748**, 136 (2012).
[14] K. Cannon, C. Hanna, and D. Keppel, Phys. Rev. D **88**, 024025 (2013).
[15] B. S. Sathyaprakash and S. V. Dhurandhar, Phys. Rev. D **44**, 3819 (1991).
[16] K. G. Arun, A. Buonanno, G. Faye, and E. Ochsner, Phys. Rev. D **79**, 104023 (2009); **84**, 049901(E) (2011).
[17] A. Buonanno, B. Iyer, E. Ochsner, Y. Pan, and B. S. Sathyaprakash, Phys. Rev. D **80**, 084043 (2009).
[18] C. K. Mishra, A. Kela, K. G. Arun, and G. Faye, Phys. Rev. D **93**, 084054 (2016).
[19] L. Blanchet, Living Rev. Relativity **17**, 2 (2014).
[20] A. Buonanno and T. Damour, Phys. Rev. D **59**, 084006 (1999).
[21] A. Buonanno and T. Damour, Phys. Rev. D **62**, 064015 (2000).
[22] T. Damour, P. Jaranowski, and G. Schaefer, Phys. Rev. D **78**, 024009 (2008).
[23] T. Damour and A. Nagar, Phys. Rev. D **79**, 081503 (2009).
[24] E. Barausse and A. Buonanno, Phys. Rev. D **81**, 084024 (2010).
[25] A. Taracchini *et al.*, Phys. Rev. D **89**, 061502 (2014).
[26] M. Pürrer, Phys. Rev. D **93**, 064041 (2016).
[27] A. Bohé *et al.*, Phys. Rev. D **95**, 044028 (2017).
[28] B. P. Abbott *et al.* (Virgo, LIGO Scientific), Phys. Rev. X **6**, 041015 (2016).
[29] B. P. Abbott *et al.* (Virgo, LIGO Scientific), Phys. Rev. Lett. **116**, 241102 (2016).
[30] B. P. Abbott *et al.* (Virgo, LIGO Scientific), Phys. Rev. Lett. **116**, 221101 (2016).
[31] Y. Pan, A. Buonanno, A. Taracchini, L. E. Kidder, A. H. Mroué, H. P. Pfeiffer, M. A. Scheel, and B. Szilágyi, Phys. Rev. D **89**, 084006 (2014).
[32] S. Babak, A. Taracchini, and A. Buonanno, Phys. Rev. D **95**, 024010 (2017).
[33] S. Husa, S. Khan, M. Hannam, M. Pürrer, F. Ohme, X. J. Forteza, and A. Bohé, Phys. Rev. D **93**, 044006 (2016).
[34] S. Khan, S. Husa, M. Hannam, F. Ohme, M. Pürrer, X. J. Forteza, and A. Bohé, Phys. Rev. D **93**, 044007 (2016).
[35] M. Hannam, P. Schmidt, A. Bohe, L. Haegel, S. Husa, F. Ohme, G. Pratten, and M. Purrer, Phys. Rev. Lett. **113**, 151101 (2014).
[36] T. B. Littenberg, J. G. Baker, A. Buonanno, and B. J. Kelly, Phys. Rev. D **87**, 104003 (2013).
[37] D. A. Brown, P. Kumar, and A. H. Nitz, Phys. Rev. D **87**, 082004 (2013).
[38] C. Capano, Y. Pan, and A. Buonanno, Phys. Rev. D **89**, 102003 (2014).
[39] I. Harry, J. C. Bustillo, and A. Nitz, Phys. Rev. D **97**, 023004 (2018).

[40] V. Varma, P. Ajith, S. Husa, J. C. Bustillo, M. Hannam, and M. Pürrer, Phys. Rev. D **90**, 124004 (2014).
[41] P. B. Graff, A. Buonanno, and B. S. Sathyaprakash, Phys. Rev. D **92**, 022002 (2015).
[42] V. Varma and P. Ajith, Phys. Rev. D **96**, 124024 (2017).
[43] J. C. Bustillo, P. Laguna, and D. Shoemaker, Phys. Rev. D **95**, 104038 (2017).
[44] B. P. Abbott *et al.* (Virgo, LIGO Scientific), Classical Quantum Gravity **34**, 104002 (2017).
[45] Y. Pan, A. Buonanno, M. Boyle, L. T. Buchman, L. E. Kidder, H. P. Pfeiffer, and M. A. Scheel, Phys. Rev. D **84**, 124052 (2011).
[46] A. K. Mehta, C. K. Mishra, V. Varma, and P. Ajith, Phys. Rev. D **96**, 124010 (2017).
[47] L. London, S. Khan, E. Fauchon-Jones, X. J. Forteza, M. Hannam, S. Husa, C. Kalaghatgi, F. Ohme, and F. Pannarale, Phys. Rev. Lett. **120**, 161102 (2018).
[48] S. Marsat (private communication).
[49] R. Fujita, Prog. Theor. Phys. **128**, 971 (2012).
[50] T. Chu, H. Fong, P. Kumar, H. P. Pfeiffer, M. Boyle, D. A. Hemberger, L. E. Kidder, M. A. Scheel, and B. Szilagyi, Classical Quantum Gravity **33**, 165001 (2016).
[51] M. Zilhão and F. Löffler, Int. J. Mod. Phys. A **28**, 1340014 (2013).
[52] F. Loffler *et al.*, Classical Quantum Gravity **29**, 115001 (2012).
[53] E. Barausse, A. Buonanno, S. A. Hughes, G. Khanna, S. O'Sullivan, and Y. Pan, Phys. Rev. D **85**, 024046 (2012).
[54] A. Taracchini, A. Buonanno, G. Khanna, and S. A. Hughes, Phys. Rev. D **90**, 084025 (2014).
[55] A. H. Mroue *et al.*, Phys. Rev. Lett. **111**, 241104 (2013).
[56] P. Kumar, T. Chu, H. Fong, H. P. Pfeiffer, M. Boyle, D. A. Hemberger, L. E. Kidder, M. A. Scheel, and B. Szilagyi, Phys. Rev. D **93**, 104050 (2016).
[57] P. Kumar, K. Barkett, S. Bhagwat, N. Afshari, D. A. Brown, G. Lovelace, M. A. Scheel, and B. Szilágyi, Phys. Rev. D **92**, 102001 (2015).
[58] G. Lovelace, M. Scheel, and B. Szilagyi, Phys. Rev. D **83**, 024010 (2011).
[59] M. A. Scheel, M. Giesler, D. A. Hemberger, G. Lovelace, K. Kuper, M. Boyle, B. Szilágyi, and L. E. Kidder, Classical Quantum Gravity **32**, 105009 (2015).
[60] A. H. Mroue *et al.*, Phys. Rev. Lett. **111**, 241104 (2013).
[61] B. Bruegmann, J. A. Gonzalez, M. Hannam, S. Husa, U. Sperhake, and W. Tichy, Phys. Rev. D **77**, 024027 (2008).
[62] S. Husa, J. A. Gonzalez, M. Hannam, B. Bruegmann, and U. Sperhake, Classical Quantum Gravity **25**, 105006 (2008).
[63] J. G. Baker, W. D. Boggs, J. Centrella, B. J. Kelly, S. T. McWilliams, and J. R. van Meter, Phys. Rev. D **78**, 044046 (2008).
[64] T. Damour and A. Nagar, Phys. Rev. D **90**, 024054 (2014).
[65] L. London, D. Shoemaker, and J. Healy, Phys. Rev. D **90**, 124032 (2014); **94**, 069902(E) (2016).
[66] W. Del Pozzo and A. Nagar, Phys. Rev. D **95**, 124034 (2017).
[67] L. T. London, arXiv:1801.08208.
[68] O. Dreyer, B. J. Kelly, B. Krishnan, L. S. Finn, D. Garrison, and R. Lopez-Aleman, Classical Quantum Gravity **21**, 787 (2004).
[69] E. Berti, V. Cardoso, and C. M. Will, Phys. Rev. D **73**, 064030 (2006).
[70] J. Meidam, M. Agathos, C. Van Den Broeck, J. Veitch, and B. S. Sathyaprakash, Phys. Rev. D **90**, 064009 (2014).
[71] H. Yang, K. Yagi, J. Blackman, L. Lehner, V. Paschalidis, F. Pretorius, and N. Yunes, Phys. Rev. Lett. **118**, 161101 (2017).
[72] L. Pekowsky, J. Healy, D. Shoemaker, and P. Laguna, Phys. Rev. D **87**, 084008 (2013).
[73] J. C. Bustillo, S. Husa, A. M. Sintes, and M. Pürrer, Phys. Rev. D **93**, 084019 (2016).
[74] D. Shoemaker (LIGO Collaboration), Advanced LIGO anticipated sensitivity curves (2010), LIGO Document T0900288-v3.
[75] J. Healy, P. Laguna, L. Pekowsky, and D. Shoemaker, Phys. Rev. D **88**, 024034 (2013).
[76] Y. Pan, A. Buonanno, R. Fujita, E. Racine, and H. Tagoshi, Phys. Rev. D **83**, 064003 (2011); **87**, 109901(E) (2013).
[77] I. Kamaretsos, M. Hannam, and B. Sathyaprakash, Phys. Rev. Lett. **109**, 141102 (2012).
[78] L. S. Finn and D. F. Chernoff, Phys. Rev. D **47**, 2198 (1993).
[79] I. Harry, S. Privitera, A. Bohé, and A. Buonanno, Phys. Rev. D **94**, 024012 (2016).
[80] A. Buonanno, Y.-b. Chen, and M. Vallisneri, Phys. Rev. D **67**, 104025 (2003); **74**, 029904(E) (2006).
[81] I. Hinder *et al.*, Classical Quantum Gravity **31**, 025012 (2014).
[82] N. W. Taylor, M. Boyle, C. Reisswig, M. A. Scheel, T. Chu, L. E. Kidder, and B. Szilágyi, Phys. Rev. D **88**, 124010 (2013).
[83] A. Buonanno, G. B. Cook, and F. Pretorius, Phys. Rev. D **75**, 124018 (2007).
[84] B. J. Kelly and J. G. Baker, Phys. Rev. D **87**, 084004 (2013).
[85] E. Berti and A. Klein, Phys. Rev. D **90**, 064012 (2014).
[86] E. Barausse and A. Buonanno, Phys. Rev. D **84**, 104027 (2011).
[87] E. Barausse, E. Racine, and A. Buonanno, Phys. Rev. D **80**, 104025 (2009); **85**, 069904(E) (2012).
[88] A. Buonanno, G. Faye, and T. Hinderer, Phys. Rev. D **87**, 044009 (2013).
[89] T. Damour and A. Nagar, Phys. Rev. D **76**, 064028 (2007).
[90] T. Damour, B. R. Iyer, and A. Nagar, Phys. Rev. D **79**, 064004 (2009).
[91] A. Nagar and A. Shah, Phys. Rev. D **94**, 104017 (2016).
[92] F. Messina, A. Maldarella, and A. Nagar, Phys. Rev. D **97**, 084016 (2018).
[93] E. Berti, V. Cardoso, and A. O. Starinets, Classical Quantum Gravity **26**, 163001 (2009).
[94] E. Barausse, V. Morozova, and L. Rezzolla, Astrophys. J. **758**, 63 (2012); **786**, 76(E) (2014).
[95] D. A. Hemberger, G. Lovelace, T. J. Loredo, L. E. Kidder, M. A. Scheel, B. Szilágyi, N. W. Taylor, and S. A. Teukolsky, Phys. Rev. D **88**, 064014 (2013).
[96] F. Hofmann, E. Barausse, and L. Rezzolla, Astrophys. J. **825**, L19 (2016).
[97] G. Faye, L. Blanchet, and B. R. Iyer, Classical Quantum Gravity **32**, 045016 (2015).

[98] R. O'Shaughnessy, B. Farr, E. Ochsner, H.-S. Cho, V. Raymond, C. Kim, and C.-H. Lee, Phys. Rev. D **89**, 102005 (2014).
[99] A. Taracchini, A. Buonanno, S. A. Hughes, and G. Khanna, Phys. Rev. D **88**, 044001 (2013); **88**, 109903(E) (2013).
[100] E. Harms, G. Lukes-Gerakopoulos, S. Bernuzzi, and A. Nagar, Phys. Rev. D **93**, 044015 (2016).
[101] E. Harms, G. Lukes-Gerakopoulos, S. Bernuzzi, and A. Nagar, Phys. Rev. D **94**, 104010 (2016).
[102] T. D. Abbott *et al.* (Virgo, LIGO Scientific), Phys. Rev. X **6**, 041014 (2016).
[103] A. Taracchini, Y. Pan, A. Buonanno, E. Barausse, M. Boyle, T. Chu, G. Lovelace, H. P. Pfeiffer, and M. A. Scheel, Phys. Rev. D **86**, 024011 (2012).
[104] T. Damour and A. Nagar, Phys. Rev. D **90**, 044018 (2014).
[105] J. Aasi *et al.* (VIRGO, LIGO Scientific), Phys. Rev. D **89**, 122003 (2014).
[106] J. Aasi *et al.* (VIRGO, LIGO Scientific), Phys. Rev. D **89**, 102006 (2014).
[107] J. Aasi *et al.* (VIRGO, LIGO Scientific), Phys. Rev. D **87**, 022002 (2013).
[108] J. Abadie *et al.* (VIRGO, LIGO Scientific), Phys. Rev. D **85**, 102004 (2012).